Tampere University

Stephen Z. D. Plachta

Multi-Qubit Quantum Finite Automata Using Structured Photons

Faculty of Engineering and Natural Sciences
Master's thesis
June 2021

ABSTRACT

Stephen Z. D. Plachta: Multi-Qubit Quantum Finite Automata Using Structured Photons
Master's thesis
Tampere University
Master's Degree Programme in Advanced Engineering Physics
June 2021

Finite automata (FA) are fundamental computational devices that make binary decisions (yes or no) using their finite memories (states) after reading a given input once, symbol by symbol. Quantum FAs (QFAs) are exponentially state-efficient compared to classical FAs when solving whether the length of an input string is a multiple of some prime number $\mathfrak{p}$: classical FAs require $\mathfrak{p}$ states, but QFAs are capable of using only log($\mathfrak{p}$) states (with small decision errors) [2]. In this work, we fix $\mathfrak{p} = 11$ and describe how an 8-state QFA in a single system analyzes an input string of identical characters a of length $\mathfrak{i}$, outputting whether or not $\mathfrak{i}$ is an integer multiple of $\mathfrak{p}$. That is, we propose a QFA system that computes $MOD_{\mathfrak{p}} = \{a^{\mathfrak{i}} | \mathfrak{i}\ mod\ \mathfrak{p} \equiv 0\}$ with $\mathfrak{p} = 11$ and $\mathfrak{i} \in \{0, ..., 11\}$.

For this purpose, we use the high-dimensional state space of spatial light modes [9]. We construct up to four qubits from two Laguerre-Gaussian (LG) modes with opposite-signed OAM quanta, e.g., $\ell = \{\pm 1, \pm 2, \pm 3, \pm 4\}$. These are the basis states of our multi-qubit QFA, whose internal state is a linear superposition of these modes. A unitary rotation operation reads one character at a time from the input string.

After $\mathfrak{n}$ rotations, the measurement of the output state computes the accepting probability, $P_{\mathfrak{n}} = |\langle \Psi_f | \Psi_i \rangle|^2$, of the final state with the initial state. The simulated accepting probability of our 8-state system is $P_{11} = 100\%$ after 11 operations and less than 12% for other nonempty strings.

Due to the physical reality (losses and inefficiencies) of the experimental system, we were limited to investigating input strings of length $\mathfrak{p} = 5$. However, the results show that 2-qubit (4-state) QFAs with $180°$ or $360°$ symmetry are capable of investigating the prime number promise problem for $\mathfrak{p} = 5$, thus demonstrating the state-space efficiency of a multi-qubit QFA using structured photons.

Keywords: quantum finite automaton, automata, qubit, high-dimensional, structured photon, spatial modes, prime number promise problem, quantum optics.

The originality of this thesis has been checked using the Turnitin Originality Check service.

I dedicate this thesis to those who ***question everything***[1], like my brother (RIP), Jonathan Livingston Seagull [4], and Isaac Newton, who said,

I do not know
what I may appear to the world,
but to myself I seem to have been
only like a boy playing on the seashore
and diverting myself in now and then finding
a smoother pebble or prettier shell
than ordinary, whilst
the great ocean of truth
lay all undiscovered before me.

With gratitude to the nice lady who saw a 12-year-old boy at a silent auction gazing longingly at a calligraphic print of the above, decorated by a seagull and a (water) wave, and asked, “Do you want that?"

[1] even what I say

ACKNOWLEDGEMENTS

First acknowledgements go wholeheartedly to Robert Fickler, whose supervision and guidance facilitate a learning environment at the Experimental Quantum Optics (EQO) group where, together with the other members of the EQO team, Rafael Barros, Subhajit Bej, Matias Eriksson, Markus Hiekkamäki, Lea Kopf, Oussama Korichi, Madona Mekhael, and Shashi Prabhakar, I can thrive. To do so while exploring fundamental questions about the nature of the universe satisfies a lifelong yearning.

In no particular order, I also acknowledge the following:

Nekhel Das, who suggested I contact Robert in the first place when we were chatting 2 years ago about possible summer research in physics; Khai Phan, for the consistent companionship in physics courses and saunas, and for reminding me to derive things from first principles; Setareh Zakeri, whose mentorship in the Talent Tampere program prepared me for PhD pursuits in physics, and who became a stellar karaoke buddy; Abuzer Yakaryilmaz, without whom this project might never have been born; and everybody in the SK1 corridor, for keeping it festive.

Our team acknowledges support from the Academy of Finland through the Competitive Funding to Strengthen University Research Profiles (decision 301820) and the Photonics Research and Innovation Flagship (PREIN–decision 320165). Robert Fickler also acknowledges support from Academy of Finland through the Academy Research Fellowship (decision 332399).

If you, dear reader, feel like your name belongs here, it does. It's a fault of my memory, not of your influence.

I am continuously grateful that my sisters and parents continue to send their love and support from across the pond. I hope I return it in equal measure.

And Aaron Carver, you sat with a curious 5-year-old boy and taught him how to add and subtract in a manner that ignited a lifelong love of mathematics. Thank you!

CONTENTS

List of Figures

SYMBOLS AND ABBREVIATIONS

δ	azimuthal phase of the transverse structure of light ($\delta = \ell\theta_r$)
ℓ	topological charge (or azimuthal index) of the transverse structure of an LG mode
$\hbar$	reduced Planck's constant
$\mathfrak{i}$	input string length
$\mathfrak{n}$	number of QFA operations (loops)
$\mathfrak{p}$	prime number of interest
ϕ	azimuthal angle coordinate of a qubit vector on the Bloch sphere (in spherical coordinates)
h	Planck's constant
θ	polar angle coordinate of a qubit vector on the Bloch sphere (in spherical coordinates)
θ_r	azimuthal angle coordinate of the transverse structure of light (in cylindrical coordinates)
o	mode order
p	radial index of the transverse structure of an LG mode
r	radial position coordinate of the transverse structure of light (in cylindrical coordinates)
w	beam radius
w_0	beam waist or minimal beam radius (at the focus of a lens)
z_R	Rayleigh length
BS	beamsplitter
CFA	classical finita automaton (automata)
DFA	deterministic finite automaton (automata)
e.g.	for example, from Latin *exempli gratia*
et al.	and others, from Latin *et alii*
FA	finite automaton (automata)
FS	fused silica

i.e.	that is, from Latin *id est*
LC	liquid crystal
LCOS	liquid crystal on silicon
LG	Laguerre-Gaussian
MUB	mutually unbiased basis
N-BK7	borosilicate glass manufactured by Schott AG
NFA	nondeterministic finite automaton (automata)
OAM	orbital angular momentum
PBS	polarizing beamsplitter
PFA	probabilistic finite automaton (automata)
ppKTP	periodically-poled potassium titanyl phosphate
PWE	paraxial wave equation
QFA	quantum finite automaton (automata)
SAM	spin angular momentum
SLM	spatial light modulator
SMF	single-mode fiber
SPDC	spontaneous parametric down-conversion

1 INTRODUCTION

Over a century of evidence has shown that the universe we live in is comprised, on the smallest scales, of bosonic[1] and fermionic[2] quanta. These quanta arise as excited states of their fields [17], which are fundamental to nature even in a vacuum. In this thesis, excitations of the electromagnetic field, photons, are used as practical tools to search for prime numbers, which are integers greater than 1 that cannot be written as the product of two smaller natural numbers.

Early observations regarding the existence of elementary quanta arose from the double-slit experiment, which shows that quanta (photons, electrons, and others) have both wave-like and particle-like behavior, moving like waves and striking like particles; the emission and absorption spectra of light by atoms, which demonstrate that electrons orbit the protons and neutrons of atomic nuclei at discrete energy levels; and the photoelectric effect, which describes how photons striking a material surface cause electrons to be ejected if and only if they carry at least the minimum quantum of energy required to free the electrons from their material bonds. These observations revealed at least two fundamental aspects of nature. The first is that a photon carries an energy, E_γ, proportional to **(a)** the rate of oscillation of its electromagnetic field, known as its frequency, ν, a continuous variable, and **(b)** Planck's constant, h, a fundamental, indivisible unit inherent to quantum reality. Put simply, $E_\gamma = h\nu$. The second aspect is that photons (and other quanta) with matching frequencies[3] can interfere in much the same way that water and sound waves do, forming patterns of bright and dark regions where constructive or destructive interference occur.

It is this second aspect, interference, that this thesis utilizes to search for prime numbers. The phenomenon is observed even when single photons are allowed to travel through a double-slit apparatus (if the slits and the distance between them are close to the photon's wavelength, $\lambda = c/\nu$, where c is the speed of light). This is because the field carries the information, described by its wavefunction, about the state of the photon, which under these conditions is indeterminate regarding which slit it went through. Until a measurement is made that asks for "which path" information, the field's wavefunction is in a superposition of both (all) possible paths. This is true for other observable variables, as well, such as linear momentum; energy and time; and amplitude and phase. The wavefunction car-

[1] photons, gluons, Higgs, Z, W, gravitons (hypothesized), and their composites

[2] quarks, leptons, their antiparticles, and their composites

[3] such as those emitted by fluorescent lights; try making a tiny slit between your thumb and forefinger and seeing the interference (single-slit diffraction) fringes that form!

ries information about all possible substates (eigenstates) that a projective measurement about some variable could result in, weighted by the probability of that substate being observed[4].

As a consequence, light fields (photons) can be manipulated to carry information in multiple dimensions across multiple degrees of freedom, including polarization (the geometry of oscillation of the electric field), spin angular momentum (SAM, nonzero for elliptical or circular polarization geometries), and orbital angular momentum (OAM, related to the spatial structure of the field around the propagation axis). The dimensional space of the OAM degrees of freedom is infinite [3].

This thesis utilizes the infinite-dimensional state space of OAM modes (shapes) to put single photons into superpositions of multiple OAM substates with some type of overall rotational symmetry. After rotating the field structure some number of times as the photon propagates, a projective measurement determines how the final state interferes with the initial state. If the structure has rotated such that it matches up with the initial structure, then perfectly constructive interference occurs. In this case, the system is said to be in an accepting state. If the structure does not align after being rotated, then some amount of destructive interference occurs. In this case, the measurement might record an accepting state and might record a rejecting state (destructive interference), with probabilities determined by the equations of Chapter 2, measured experimentally by the methods of Chapter 3, and reported in Chapter 4.

If the system is in an accepting state after a number of rotations equal to the prime number of interest, then the prime number search has succeeded. If the system is measured to be in an accepting state after a number of rotations not equal to the prime number of interest, then the system has made a decision error. The goal of this work is to minimize the decision errors such that the results compare favorably with similar prime number searches performed by classical (non-quantum) systems.

[4] probabilities which Einstein famously lamented in his conviction that a fully deterministic theory would emerge that "does not throw dice with the universe" [8].

2 THEORY

In this chapter I describe the underlying theory necessary to explain the system used to realize a four-qubit quantum finite automaton (QFA). I do so using the subjects of formal languages (as described in mathematics and computer science), finite automata (FA), electromagnetic fields (both classical and quantum), and the transverse structure of light. These theories explain the methods chosen and the observations made, described in Chapters 3 and 4, respectively.

2.1 Formal Language

A language is defined as the set of all strings (words) that can be concatenated from an alphabet in ways that follow a certain set of rules. An alphabet is an set of symbols, letters, or tokens whose elements can be used to convey information via a language. Two examples are the English alphabet $A_E = \{a, ..., z\}$ and the alphabet used in elementary arithmetic, formally $A_A = \{0, \dots, 9\} \cup \{+, \times, -, \div, =\} \cup \{), (\}$ [15].

The set of all possible finite sequences of words is represented as A^*. Only some sequences produce meaningful strings that comply with the rules (grammar or mathematical operations), a subset of A^* called the language $\mathcal{L}$. Other members of A^* produce sequences that do not comply with the rules, e.g., nonsense words or invalid mathematical expressions; these are not included in the language.

A simple means of generating a language involves decision problems, which have a binary output 'yes' or 'no.' They are applied when computing, for example, whether a password is valid or an email address has an acceptable syntax.

One particular class of decision problems is called promise problems, which determine whether an input is a member of some subset of possible inputs. This thesis researches the prime number promise problem, which aims to answer whether an integer input is a multiple of a prime number. Using strings, this question can be investigated with the input alphabet $A = \{a\}$, where the only valid strings are sequences of a's represented as $a^{\mathfrak{i}}$, where $\mathfrak{i}$ is the number of a's in the string. For $\mathfrak{i} = 0$, the empty string is denoted ε.

2.2 Finite Automata (FA)

In this thesis, a machine known as a finite automaton (FA) will determine whether $\mathfrak{i}$ is an integer multiple of some prime number $\mathfrak{p}$. In other words, an algorithm will compute the members of the language $A_M = MOD_{\mathfrak{p}} = \{a^{\mathfrak{i}} | \mathfrak{i} \bmod(\mathfrak{p}) \equiv 0\} \in A$.

In general, an FA takes an input, reads it symbol by symbol, performs an input-dependent operation on its state after each step, and outputs a member of the binary alphabet $A_O = \{0, 1\}$. An FA is therefore a perfect tool to solve decision problems. For the prime number promise problem, because each input of the string $a^{\mathfrak{i}}$ is identical, an FA performs the same operation for each character read.

In language theory, which classifies algorithms based on the type of memory used to implement their task, algorithms that an FA can implement are the simplest. Algorithms can also be classified by other means, such as the running time criterion employed by complexity theory [15].

2.2.1 Classical Finite Automata (CFA)

A classical finite automaton (CFA) can be deterministic (DFA) or nondeterministic (NFA). If it is deterministic, then it obeys two conditions: each character read by the machine causes a unique transition of its internal state (to the current state or to a new one), and it must read an input symbol to perform an operation.

If a CFA is nondeterministic, then these requirements do not apply. That is, a unique character read by an NFA might lead arbitrarily to multiple possible (same or different) states, and some NFAs might operate on their internal states after reading an empty string ε. Thereby, reading the same string multiple times can produce different results in A_O in a nondeterministic manner, but if any of the possible runs produces an accepting state, then the input is accepted. Equivalently, any step where a forked decision is possible causes the machine to copy itself into each transition, and the input is only rejected if no copy is in an accepting state after the input is consumed. A process called subset (or powerset) construction can be used to convert any NFA into a DFA, as detailed in [19]. Any language accepted by an NFA can therefore be represented by an equivalent DFA. These are the regular languages [15].

An NFA can be generalized to a probabilistic finite automaton (PFA) by representing the current state and each transition operator (and their probabilities) by real-valued stochastic vectors and matrices, respectively. In a PFA, the possible states and transitions have definite probabilities assigned to them [18]. Computations by PFAs result in the stochastic languages, an uncountable set containing the regular languages as a subset.

To solve the prime number promise problem classically, a DFA can be used. It requires at least $\mathfrak{p}$ distinct memory states [13]. Each one stores a unique remainder of $\mathfrak{i} \bmod(\mathfrak{p})$,

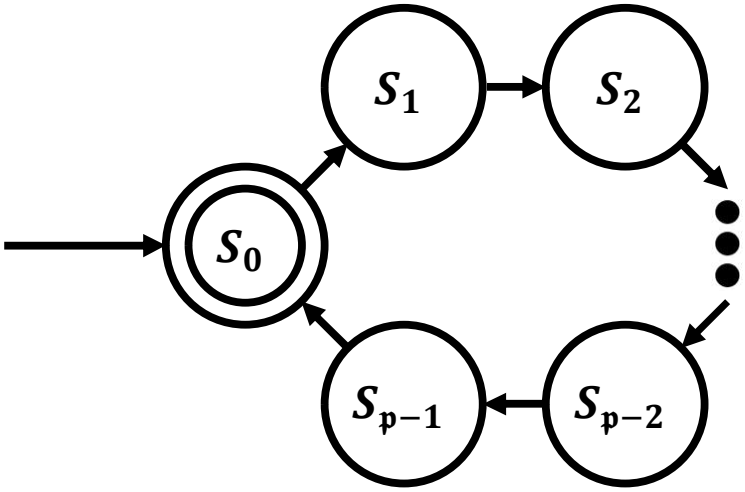

Figure 2.1 A DFA state diagram. This $\mathfrak{p}$-state DFA answers the prime number promise problem for a prime number $\mathfrak{p}$. Each character read from the input string advances the automaton's internal state by 1. For $\mathfrak{n} \in \{0, ..., \infty\}$, any string $a^{\mathfrak{i}}$ with $\mathfrak{i} = \mathfrak{n} \cdot \mathfrak{p}$ is accepted, and the automaton returns to its initial state S_0 (the only accepting state, marked by a double circle). Note that the empty string, $a^0 = \varepsilon$, is accepted.

counting the symbols until a return to an integer multiple of $\mathfrak{p}$. Figure 2.1 represents this with a map: for $\mathfrak{n} \in \{0, ..., \mathfrak{p}\}$, if $\mathfrak{n}$ characters have been read, then the $\mathfrak{n}^{\text{th}}$ state $S_{\mathfrak{n}}$ has a bit value of 1, while all others read 0. This cycle repeats after every $\mathfrak{p}^{\text{th}}$ character. The system outputs 1 (accepted) if and only if $S_0 = 1$ at the end of a string. Note that a 2-state DFA can answer whether a number is even.

2.2.2 Quantum Finite Automata (QFA)

Certain calculations can be performed more efficiently in terms of time and/or memory states with a system whose state is a superposition of multiple sub-states, as can be done with quantum systems. This comes with the cost, as mentioned in the Introduction (Chapter 1), of decision errors caused by probabilistic outputs $0 \leq P \leq 1$.

Any functional QFA, mapped in Figure 2.2a, has a nonzero probability of answering 'yes' when the answer is actually 'no'[1]. The primary question for practical calculations then becomes, "What error threshold is acceptable for the task at hand?" Theoretically, the error bound can be any value less than $1/2$. Depending on the application, better bounds may be proposed or used. In complexity theory, the error bound $1/3$ is widely used to define the standard complexity classes (see, e.g., page 397 of the standard textbook [21] or the survey [22]).

For a QFA investigating the prime number promise problem, mapped in Figure 2.2b,

[1]It is therefore a quantum analog of a PFA, though here the state vectors and transition matrices can be complex-valued and the matrices are unitary, as discussed in Section 2.2.2.1.

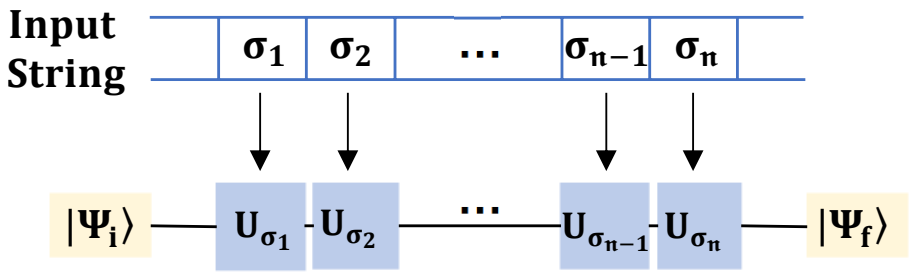

(a)

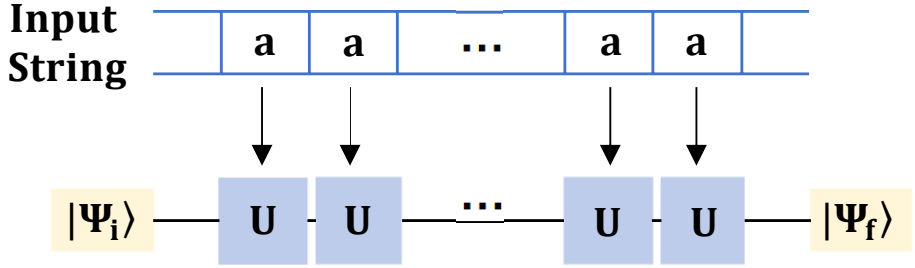

(b)

Figure 2.2 QFA state diagrams. **(a)** A general state diagram. Each unique character of an input string read by a QFA leads to a different unitary operation U_{σ_i} being performed on the QFA's internal state. **(b)** The QFA state diagram for the prime number promise problem. The input string is in the alphabet $A = \{a\}$, so each unitary operator U is identical. A projective measurement of a QFA's output state, $\langle \Psi_f | \Psi_i \rangle \in [-1, 1]$, has an accepting probability $0 \leq |\langle \Psi_f | \Psi_i \rangle|^2 \leq 1$.

a slightly better error bound of $1/4$ is chosen to ensure practical usefulness, where the candidate integers can be further investigated classically to achieve certainty. The use of the QFA becomes superior to the use of a DFA if the prime number search is more efficient in time and/or in state space. In fact, while a DFA requires $\mathfrak{p}$ states to solve the prime number promise problem, a QFA can examine it using a number of states on the order of $\log \mathfrak{p}$, that is $\mathcal{O}(\log \mathfrak{p})$ [2].

The next section explains how to achieve this exponential state efficiency using a multi-qubit (quantum bit) system.

2.2.2.1 Quantum states and qubits

This thesis adopts Dirac notation to represent the state vectors of the QFA system and its sub-automata (qubits) in terms of bras and kets. A qubit is a member state of the two-dimensional complex Hilbert space $\mathcal{H}$.

In spherical coordinates on the unit sphere (Bloch sphere), a qubit state in $\mathcal{H}$ is in general represented:

$$|\psi\rangle = \cos(\theta/2)\begin{pmatrix}1\\0\end{pmatrix} + e^{i\phi}\sin(\theta/2)\begin{pmatrix}0\\1\end{pmatrix} = \cos(\theta/2)\,|0\rangle_c + e^{i\phi}\sin(\theta/2)\,|1\rangle_c\,, \qquad (2.1)$$

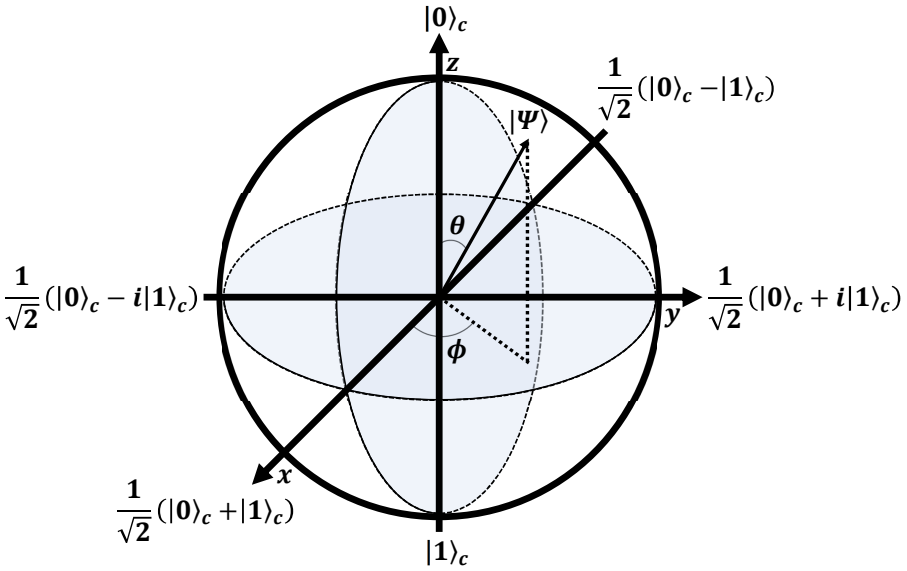

Figure 2.3 Bloch sphere representation of complex qubit vectors in two-dimensional Hilbert space. The state $|\Psi\rangle$ of Equation (2.1) is shown, with the computational basis state vectors at the poles of the z-axis and their equally-weighted superpositions along the equator.

where the polar angle $0 \leq \theta \leq \pi$, the azimuthal angle $0 \leq \phi \leq 2\pi$, and i is the imaginary unit. The subscript c refers to the computational basis; it is introduced to eliminate ambiguity with later notation.

General qubits represented by Equation (2.1) are pure 2-dimensional quantum states that map in terms of complex, normalized vectors to the surface of the Bloch sphere, as shown in Figure 2.3. Any unitary matrix operation acting on $|\psi\rangle$ represents a transformation of the qubit vector from one position on the Bloch sphere to another. Mixed quantum states lie within the Bloch sphere, with vector magnitudes less than 1, with a completely mixed state being in the center. The states used in this work are pure, comprised of up to four qubits in coherent superpositions, each represented on its own independent Bloch sphere.

The computational basis state vectors, represented in Equation (2.1) by $|0\rangle_c$ and $|1\rangle_c$, are positioned at the north and south poles along the z-axis of the Bloch sphere. They are mutually exclusive states of some physical property of a system, e.g., the upward and downward z-components of the spin (angular momentum due to magnetic moment) of an electron in a magnetic field or the horizontal and vertical polarization states of a photon.

A qubit represented by Equation (2.1) is in a linear superposition of the computational basis states; a projective measurement of the physical property it represents will yield $|0\rangle_c$ with probability $|\cos(\theta/2)|^2$ and $|1\rangle_c$ with probability $|\sin(\theta/2)|^2$.

While qubits can perform calculations in the computational basis, equally valid are two other bases for which a measurement made in one basis yields no information about the possible results of measurements in the other bases. These bases are represented

by pairs of vectors pointing in opposite directions along the x- and y-axes of the Bloch sphere. Together, the three bases comprise a set of mutually unbiased bases (MUBs). They can be represented:

$$|0\rangle_c, |1\rangle_c;\ \frac{1}{\sqrt{2}}(|0\rangle_c + |1\rangle_c), \frac{1}{\sqrt{2}}(|0\rangle_c - |1\rangle_c);\ \frac{1}{\sqrt{2}}(|0\rangle_c + i\,|1\rangle_c), \frac{1}{\sqrt{2}}(|0\rangle_c - i\,|1\rangle_c). \quad (2.2)$$

In the QFA system examined here, the second basis (defined as b_2) is selected such that the qubit basis states are $|0\rangle_{b_2} = (|0\rangle_c + |1\rangle_c)/\sqrt{2}$ and $|1\rangle_{b_2} = (|0\rangle_c - |1\rangle_c)/\sqrt{2}$. The four qubits, or sub-automata, are represented as pairs of two-dimensional mutually exclusive basis states M_j:

$$M_1 = \{|0\rangle, |1\rangle\};\ M_2 = \{|2\rangle, |3\rangle\};\ M_3 = \{|4\rangle, |5\rangle\};\ M_4 = \{|6\rangle, |7\rangle\}, \quad (2.3)$$

with each qubit M_j having x-axis (b_2) basis states distinct from every other's, written for example $|0\rangle_{M_2} = |2\rangle$ and $|1\rangle_{M_2} = |3\rangle$.

The QFA system begins with a single quantum in some state $|0\rangle_q$ that can be physically changed. The changes are represented by matrix operators. To transform $|0\rangle_q$ into the four-qubit superposition state and utilize the eight basis states in Equation (2.3), the unitary operator U_0 is applied:

$$U_0 |0\rangle_q = H \otimes H \otimes I \ |0\rangle_q$$

$$= \begin{pmatrix} \frac{1}{\sqrt{2}} & \frac{1}{\sqrt{2}} \\ \frac{1}{\sqrt{2}} & -\frac{1}{\sqrt{2}} \end{pmatrix} \otimes \begin{pmatrix} \frac{1}{\sqrt{2}} & \frac{1}{\sqrt{2}} \\ \frac{1}{\sqrt{2}} & -\frac{1}{\sqrt{2}} \end{pmatrix} \otimes \begin{pmatrix} 1 & 0 \\ 0 & 1 \end{pmatrix} |0\rangle_q$$

$$= \left(\begin{array}{cc|cc} \frac{1}{\sqrt{2}} & \frac{1}{\sqrt{2}} & \frac{1}{\sqrt{2}} & \frac{1}{\sqrt{2}} \\ \frac{1}{\sqrt{2}} & -\frac{1}{\sqrt{2}} & \frac{1}{\sqrt{2}} & -\frac{1}{\sqrt{2}} \\ \hline \frac{1}{\sqrt{2}} & \frac{1}{\sqrt{2}} & -\frac{1}{\sqrt{2}} & -\frac{1}{\sqrt{2}} \\ \frac{1}{\sqrt{2}} & -\frac{1}{\sqrt{2}} & -\frac{1}{\sqrt{2}} & \frac{1}{\sqrt{2}} \end{array}\right) \otimes \begin{pmatrix} 1 & 0 \\ 0 & 1 \end{pmatrix} |0\rangle_q$$

$$U_0 \left|0\right\rangle_q = \left(\begin{array}{cc|cc|cc|cc} \frac{1}{2} & 0 & \frac{1}{2} & 0 & \frac{1}{2} & 0 & \frac{1}{2} & 0 \\ 0 & \frac{1}{2} & 0 & \frac{1}{2} & 0 & \frac{1}{2} & 0 & \frac{1}{2} \\ \hline \frac{1}{2} & 0 & -\frac{1}{2} & 0 & \frac{1}{2} & 0 & -\frac{1}{2} & 0 \\ 0 & \frac{1}{2} & 0 & -\frac{1}{2} & 0 & \frac{1}{2} & 0 & -\frac{1}{2} \\ \hline \frac{1}{2} & 0 & \frac{1}{2} & 0 & -\frac{1}{2} & 0 & -\frac{1}{2} & 0 \\ 0 & \frac{1}{2} & 0 & \frac{1}{2} & 0 & -\frac{1}{2} & 0 & -\frac{1}{2} \\ \hline \frac{1}{2} & 0 & -\frac{1}{2} & 0 & -\frac{1}{2} & 0 & \frac{1}{2} & 0 \\ 0 & \frac{1}{2} & 0 & -\frac{1}{2} & 0 & -\frac{1}{2} & 0 & \frac{1}{2} \end{array}\right) \left|0\right\rangle_q , \tag{2.4}$$

where H is the Hadamard operator, which acts to transform $\left|0\right\rangle_c$ to $\left|0\right\rangle_{M_j} = (\left|0\right\rangle_c + \left|1\right\rangle_c)/\sqrt{2}$ and $\left|1\right\rangle_c$ to $\left|1\right\rangle_{M_j} = (\left|0\right\rangle_c - \left|1\right\rangle_c)/\sqrt{2}$; $\otimes$ is the Kronecker product; and I is the identity matrix.

The four-qubit superposition now represents the overall state of the system:

$$\left|\Psi\right\rangle = U_0 \left|0\right\rangle_q = \frac{1}{2}\left(\begin{array}{c} M_1 \\ \hline M_2 \\ \hline M_3 \\ \hline M_4 \end{array}\right) = \frac{1}{2}\left(\begin{array}{c} \cos(\theta_1/2) \\ \hline -i\,\sin(\theta_1/2) \\ \hline \cos(\theta_2/2) \\ \hline -i\,\sin(\theta_2/2) \\ \hline \cos(\theta_3/2) \\ \hline -i\,\sin(\theta_3/2) \\ \hline \cos(\theta_4/2) \\ \hline -i\,\sin(\theta_4/2) \end{array}\right). \tag{2.5}$$

By initializing each qubit to $\left|0\right\rangle_{M_j}$, the QFA state becomes:

$$\left|\Psi_i\right\rangle = \frac{1}{2}(\left|0\right\rangle + \left|2\right\rangle + \left|4\right\rangle + \left|6\right\rangle) = \frac{1}{2}\left(\begin{array}{c} 1 \\ \hline 0 \\ \hline 1 \\ \hline 0 \\ \hline 1 \\ \hline 0 \\ \hline 1 \\ \hline 0 \end{array}\right). \tag{2.6}$$

The system is in each sub-automaton with probability $1/4$ (amplitude $1/2$).

The prime number promise problem can be rephrased as the question: do $\mathfrak{n}$ identical operations return the system to its initial state, $|\Psi_i\rangle$? That is, after $\mathfrak{n}$ applications of a unitary matrix transformation U to $|\Psi_i\rangle$, does the final state match the input state, i.e., $|\langle\Psi_f|\Psi_i\rangle|^2 = 1$?

The unitary operator utilized here is the rotational matrix operator:

$$R_{k_j} = \begin{pmatrix} \cos(\phi_{k_j}) & -i\,\sin(\phi_{k_j}) \\ -i\,\sin(\phi_{k_j}) & \cos(\phi_{k_j}) \end{pmatrix}, \tag{2.7}$$

where $\phi_{k_j} = k_j \frac{2\pi}{\mathfrak{p}}$ and $1 \leq k_j < \mathfrak{p}$. The operator R_{k_j} rotates a qubit vector by ϕ_{k_j} around the z-axis of the Bloch sphere such that the qubit states remain in the xy-plane, also seen as the complex unit circle. It acts on each qubit M_j:

$$R(k_1, k_2, k_3, k_4)\,|\Psi_i\rangle = \begin{pmatrix} R_{k_1} & 0 & 0 & 0 \\ 0 & R_{k_2} & 0 & 0 \\ 0 & 0 & R_{k_3} & 0 \\ 0 & 0 & 0 & R_{k_4} \end{pmatrix} |\Psi_i\rangle\,. \tag{2.8}$$

Each operation of R on $|\Psi_i\rangle$ is the act of reading one character from the input string $a^{\mathfrak{i}}$. After $\mathfrak{n}$ operations, and employing François Viéte's formulae for $\sin(\mathfrak{n}x)$ and $\cos(\mathfrak{n}x)$, the final state becomes:

$$|\Psi_f\rangle = R_{k_j}^{\mathfrak{n}}\,|\Psi_i\rangle = |u_{\mathfrak{n}}\rangle = \frac{1}{2} \begin{pmatrix} \cos(\mathfrak{n}k_1\frac{2\pi}{\mathfrak{p}}) \\ -i\,\sin(\mathfrak{n}k_1\frac{2\pi}{\mathfrak{p}}) \\ \hline \cos(\mathfrak{n}k_2\frac{2\pi}{\mathfrak{p}}) \\ -i\,\sin(\mathfrak{n}k_2\frac{2\pi}{\mathfrak{p}}) \\ \hline \cos(\mathfrak{n}k_3\frac{2\pi}{\mathfrak{p}}) \\ -i\,\sin(\mathfrak{n}k_3\frac{2\pi}{\mathfrak{p}}) \\ \hline \cos(\mathfrak{n}k_4\frac{2\pi}{\mathfrak{p}}) \\ -i\,\sin(\mathfrak{n}k_4\frac{2\pi}{\mathfrak{p}}) \end{pmatrix}. \tag{2.9}$$

In post-processing, the application of U_0^{-1} to the final state allows a measurement in the computational basis. There are two cases: in case 1), where ($\mathfrak{n} \equiv 0 \bmod(\mathfrak{p})$), all four qubits are again in $|0\rangle_{b_2}$ along the $+x$-axis, so $U_0^{-1}\,|u_{\mathfrak{n}}\rangle = |0\rangle_q$ and the accepting probability $|\langle\Psi_f|\Psi_i\rangle|^2 = 1$; in case 2), where ($\mathfrak{n} \neq 0 \bmod(\mathfrak{p})$), at least one qubit is not in $|0\rangle_{b_2}$ and $U_0^{-1}\,|u_{\mathfrak{n}}\rangle \neq |0\rangle_q$. If any state $|j\rangle \neq |0\rangle_q$ is observed, then the QFA rejects

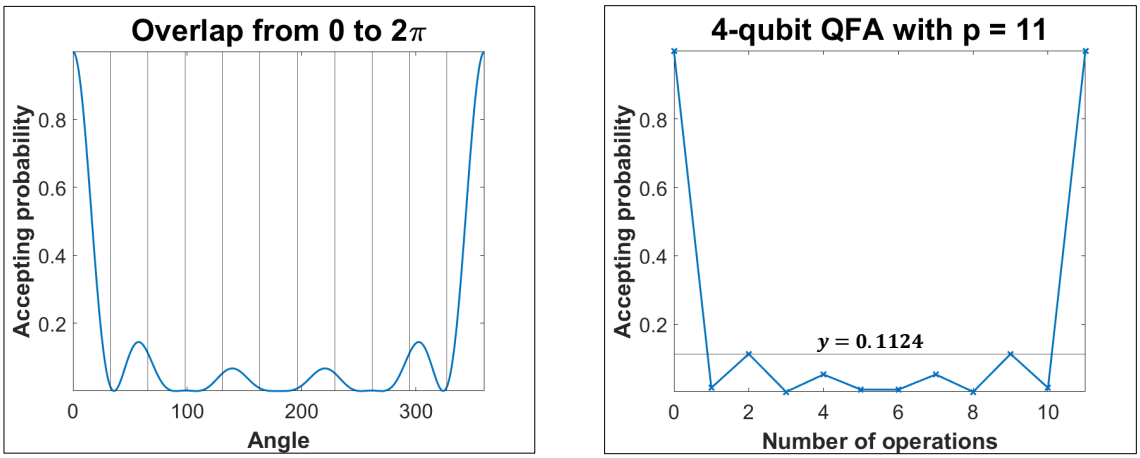

(a) **(b)**

Figure 2.4 Simulated accepting probabilities for a four-qubit QFA. **(a)** The overlap squared of the 4-qubit QFA for each angle from $0°$ to $360°$. Vertical lines indicate each $\mathfrak{n} \cdot 360°/11$. **(b)** For the prime number promise problem with $\mathfrak{p} = 11$, this discrete set of angles ensures an erroneous accepting probability of less than 12%.

$|u_{\mathfrak{n}}\rangle$. However, both $|0\rangle_q$ and the qubit states could be observed with nonzero probabilities dependent on ϕ_{k_j}.

Therefore, the critical question is, "which values of k_j maximize the rejecting probability in case 2)?" Figure 2.4a shows simulated accepting probabilities for $\{k_1, k_2, k_3, k_4\} = \{1, 2, 3, 4\}$ for every integer angle from $0°$ to $360°$. For the prime number $\mathfrak{p} = 11$, where each rotation angle is ~$32.7°$, computations shown in Figure 2.4b demonstrate that these k_j ensure a rejecting probability greater than 0.8876. Other choices of k_j, such as $\{k_j\} = \{k_1, k_2, k_3, k_4\} = \{1, 2, 4, 8\}$, produce similar results for $\mathfrak{p} = 11$ but higher peaks for angles outside of the discrete set $\mathfrak{n} \cdot 2\pi/11$, so were not chosen for measurement to reduce the possibility of experimental error.

This section described a four-qubit QFA in terms of general quantum states. In principle, this QFA could be built from any qubits, including those made from electronic, atomic, or photonic states. The next section introduces, from a classical perspective, the high-dimensional state space of the transverse spatial modes of electromagnetic fields. It then describes how to utilize the orbital angular momentum (OAM) state space of these modes, encoded onto the structure of quantized electromagnetic fields (photons), as a functional QFA to answer the prime number promise problem with $\mathfrak{p} = 11$.

2.3 Light Waves and Quanta

The classical (wave-like) and quantum (particle-like) properties of the electromagnetic field are well-established in the literature [10, 14] and textbooks [3].

Maxwell's equations successfully describe the physical properties of the electromagnetic field from the classical point of view. A monochromatic wave propagating in the z-direction in a simple dielectric medium is represented by the well-known wave equation, which describes its electric and magnetic field components. Writing the amplitude and phase of the oscillating real-valued fields in terms of complex phasors allows the wave equation to simplify to the Helmholtz equation. A further simplification, known as the paraxial approximation, is valid for light fields whose amplitudes vary slowly as they propagate in optical systems that do not diverge or focus the fields at angles of greater than about $30°$ [20]. The paraxial approximation is therefore a sufficient theoretical model for the behavior of light in the experimental conditions of this thesis, optical systems that guide collimated beams on well-defined focusing and reimaging paraxial beam paths.

2.3.1 The Paraxial Wave Equation

Assuming uniform electric and magnetic field vectors, a general formula for the time-independent complex amplitude of an electromagnetic wave is:

$$U(\mathbf{r}) = u(\mathbf{r})\exp(ikz), \tag{2.10}$$

where z is the propagation direction and $\mathbf{r}$ is the three-dimensional spatial coordinate. The phase term $\exp(ikz)$ describes the oscillation rate of the electromagnetic field, dependent on the wavenumber $k = 2\pi/\lambda$, where λ is the monochromatic wavelength. In the slowly-varying amplitude approximation, which is valid if the change in amplitude remains small for $\Delta z \approx \lambda$, the phase term is the only significant z-dependent effect. That is, if $\Delta u \ll u$, then the complex amplitude is well-characterized as a scalar wave traveling in the z-direction whose envelope u describes its modulation. This approximation simplifies the Helmholtz equation to the paraxial wave equation (PWE) [3]:

$$\left(\Delta_\perp + 2ik\frac{\partial}{\partial z}\right) u(\mathbf{s}, z) = 0, \tag{2.11}$$

where $\Delta_\perp$ is the transverse Laplacian operator and $\mathbf{s}$ is the transverse position.

The solutions of the PWE describe the transverse spatial structure of light as it propagates along an optical axis under the small-angle approximation.

2.3.2 Transverse Spatial Modes

Different families of structures of u, or spatial modes, arise from solutions to the PWE (2.11) in different coordinate systems. The Gaussian mode families are analytical solutions that are applicable to situations in optics that satisfy the small-angle constraints.

Each set of these modes is complete and orthogonal, comprised of an infinite number of basis states (modes). Superpositions of Gaussian modes can describe any paraxial beam with vanishing boundary conditions, i.e., $u(\mathbf{s}, z) \to 0$ as $\mathbf{s}, z \to \infty$. In Cartesian coordinates, $\mathbf{s} = (x, y)$, the solutions are known as Hermite-Gaussian modes. In elliptical coordinates, $\mathbf{s} = (u, v)$, the Ince-Gauss modes result. In cylindrical coordinates, $\mathbf{s} = (r, \theta_r)$, where r is the radial distance and θ_r is the azimuthal angle of the spatial structure[2], the solutions are called Laguerre-Gaussian (LG) modes. The QFA system researched in this thesis uses LG modes, so they are detailed here.

The LG spatial modes are rotationally symmetric, described by the equation:

$$\begin{aligned} LG_{\ell,p} \coloneqq u_{\ell,p}(r, \theta_r, z) = & \frac{\sqrt{2p!}}{\sqrt{\pi(|\ell| + p)!}} \frac{1}{w(z)} \left(\frac{\sqrt{2}r}{w(z)} \right)^{|\ell|} L_p^{|\ell|} \left(\frac{2r^2}{w^2(z)} \right) \\ & \cdot \exp \left[\frac{ikr^2}{2R(z)} - \frac{r^2}{w^2(z)} \right] e^{i\psi_{\ell,p}} e^{i\ell\theta_r}, \end{aligned} \tag{2.12}$$

where $w(z) = w_0(1 + (z/z_R)^2)^{1/2}$ is the beam radius (the r-value where the normalized intensity is $1/e^2$) at a distance z from its narrowest point, the beam waist w_0; $z_R = \pi w_0^2/\lambda$ is the Rayleigh length, where $w(z_R) = \sqrt{2}w_0$; and $R(z) = z(1 + z_R^2/z^2)$ is the radius of curvature of the wavefront.

One component of Equation (2.12) is the Laguerre polynomials, $L_p^{|\ell|}$, which follow the equation:

$$L_p^{\ell}(r) = \frac{e^r r^{-\ell}}{p!} \frac{d^p}{dr^p} \left(e^{-r} r^{\ell+p} \right), \tag{2.13}$$

where the characteristic numbers $\ell \in \mathbb{Z}$ and $p \in \mathbb{N}$ define the azimuthal phase structure and radial π-phase steps of the modes, respectively.

As shown in Figure 2.5, in the transverse structure of the field at any point z, if $p > 0$, then there are p ring-shaped phase jumps (black rings); if the topological charge $\ell \neq 0$, then there are $|\ell|$ phase periods from 0 to 2π in one full rotation of the azimuthal angle. That is, the azimuthal phase is $\delta = \ell\theta_r$, with the chirality defined by the sign of ℓ. This phase has a helical structure corresponding to orbital angular momentum (OAM), with each photon carrying, for linearly polarized light, an OAM value of $\ell\hbar$ [1].

If light is circularly polarized, then the angular momentum has a spin component of $\pm\hbar$ per photon, with the sign corresponding to the polarization's chirality (left- or right-handed). An elliptically polarized photon is in a superposition of left- and right-handed circular polarizations, so a projective measurement in the spin angular momentum (SAM) basis has unequal probabilities of resulting in $+\hbar$ or $-\hbar$. The angular momentum can be transferred to an absorbing particle, resulting in torque, with SAM causing it to spin about its own axis and OAM causing spin around the optical axis [10].

[2] not a Bloch sphere coordinate

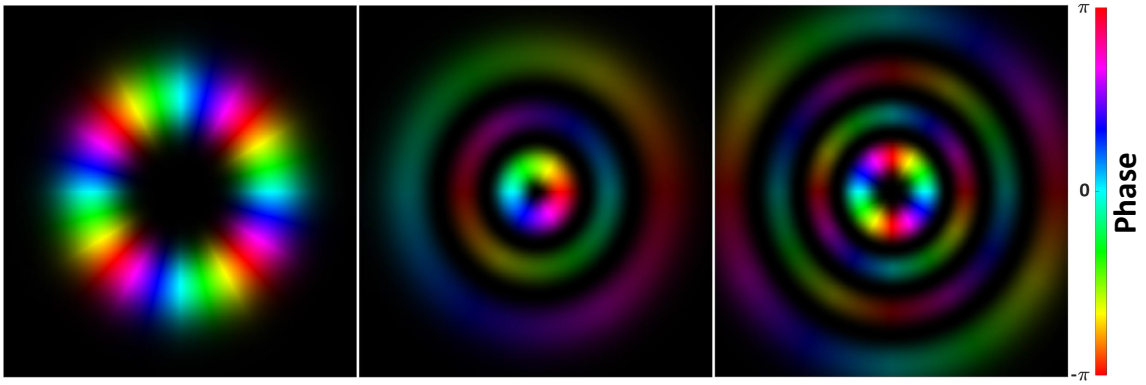

Figure 2.5 Example LG modes with, from left to right: ($\ell = 4,\ p = 0$); ($\ell = -1,\ p = 2$); ($\ell = 2,\ p = 3$). The color spectrum represents the azimuthal phase $\delta = \ell\theta_r$ from $-\pi$ to π, with the brightness representing the intensity.

The term $\psi_{\ell,p}$ in Equation (2.12) is the mode-dependent Gouy phase shift, which is imparted to the field as it propagates:

$$\psi_{\ell,p} = (|\ell| + 2p + 1)\text{arctan}(z/z_R) = (o+1)\text{arctan}(z/z_R). \tag{2.14}$$

Here $o = |\ell| + 2p$ is introduced as the mode order. For $\ell = p = 0$, the lowest-order or plain Gaussian mode is seen:

$$u_g(r, \theta_r, z) = e^{i\psi(z)} \frac{\sqrt{2}}{\sqrt{\pi} w(z)} \exp\left[\frac{ikr^2}{2R(z)} - \frac{r^2}{w^2(z)}\right], \tag{2.15}$$

where $\psi(z) = \text{arctan}(z/z_R)$, the fundamental Gouy phase shift. A general version is found by replacing $r, \theta_r \to \mathbf{s}$ and $r^2 \to |\mathbf{s}|^2$, revealing the commonality of the plain mode to Gaussian mode families in any coordinate system.

In this thesis, all LG modes used have $p = 0$, so Equation (2.13) simplifies to 1. Equations (2.12) and (2.14) can also be simplified:

$$\begin{aligned} u_{\ell,0}(r, \theta_r, z) = u_\ell(r, \theta_r, z) = &\frac{\sqrt{2}}{\sqrt{\pi|\ell|!}} \frac{1}{w(z)} \left(\frac{\sqrt{2}r}{w(z)}\right)^{|\ell|} \\ &\cdot \exp\left[\frac{ikr^2}{2R(z)} - \frac{r^2}{w^2(z)}\right] e^{i\psi_{\ell,0}} e^{i\ell\theta_r} \end{aligned} \tag{2.16}$$

$$\psi_{\ell,0} = \psi_\ell = (|\ell| + 1)\text{arctan}(z/z_R) = (o+1)\text{arctan}(z/z_R). \tag{2.17}$$

Note that the mode order becomes $o = |\ell|$.

Up to this point, the equations describing the electromagnetic field have been formulated in the classical regime, where the light field structure is seen as the intensity pattern of a beam. In the quantum regime, where light fields can be resolved into discrete quanta

(photons), the spatial structure manifests as a probability distribution. That is, a measurement of an individual photon's transverse position has a probability governed by the same pattern as the intensity of a beam in the same mode. Over time, a detector in some z-position in the path of a stream of photons builds up the same pattern as a single snapshot of an equivalent-mode beam in the same z-position.

I will now formulate a description of a four-qubit, single-photon QFA built from the higher-order OAM basis states that arise when opposite-signed OAM modes with the same topological charge are superposed.

2.3.2.1 The Photonic QFA

In terms of quantum states, the infinite, discrete, self-similar basis sets in paraxial wave space are in general:

$$|\psi_{parax}\rangle = \sum_j c_j \, |u_j\rangle \, , \tag{2.18}$$

where c_j is a coefficient deciding the probability amplitude of detecting a photon in mode $|u_j\rangle$. The orthonormality condition is satisfied:

$$\langle u_j | u_k \rangle = \iint d\mathbf{s} \; u_j^*(\mathbf{s}, z) \; u_k(\mathbf{s}, z) = \delta_{jk}, \tag{2.19}$$

where δ_{jk} is the Kronecker delta.

It is possible to superpose different modes (basis states). A general superposition between basis states from the same mode family at a focal point $z = 0$ is written:

$$|u(r, \theta_r, 0)\rangle = |u(0)\rangle = \frac{1}{\sqrt{2}}(|u_j\rangle + |u_k\rangle), \tag{2.20}$$

which have mode orders o_j and o_k contributing to the Gouy phase $\psi_j(z) \equiv (o_j + 1)\psi(z)$. At a distance z from the focal point, the state becomes:

$$\begin{aligned} |u(z)\rangle &= \frac{1}{\sqrt{2}}(e^{i\psi_j(z)} \, |u_j\rangle + e^{i\psi_k(z)} \, |u_k\rangle) \\ &= \frac{1}{\sqrt{2}} e^{i\psi_j(z)} (|u_j\rangle + e^{i(o_k - o_j)\psi(z)} \, |u_k\rangle), \end{aligned} \tag{2.21}$$

where $\psi_j(z)$ is now a global phase with no physical significance for the QFA system; only those state pairs with $o_j \neq o_k$ possess a relative phase. In such a case, the field is in a nondegenerate superposition, and the evolution of the field state with propagation along the z-axis includes variations in the interference between different substates that appear as complex changes in the transverse structure. If each mode has the same mode order, i.e., $o_j = o_k$, then they are said to belong to the same mode generation. The transverse

structure is then self-similar along the z-axis. That is, the structure does not change apart from focusing and divergence. This is often called a degenerate superposition [14].

As mentioned in Equation (2.17), the basis states used in this thesis have mode order $o_j = |\ell_j|$. A qubit-state superposition of LG modes of this type is:

$$|\psi_{LG}\rangle = \cos(\theta/2)\,|LG_{\ell,p}\rangle + e^{i\phi}\sin(\theta/2)\,|LG_{-\ell,p}\rangle\,, \tag{2.22}$$

which for $p = 0$ can be rewritten for brevity as

$$|\psi_{L}\rangle = \cos(\theta/2)\,|L_{\ell}\rangle + e^{i\phi}\sin(\theta/2)\,|L_{-\ell}\rangle\,. \tag{2.23}$$

All qubits M_j used will be degenerate, formed from pairs of OAM basis states with $\ell_j = -\ell_k$, so that the state pairs belong to the same mode order and are self-similar with z-propagation. The relative phase between different qubits depends on the Gouy phase, which changes at different rates for different qubits, but this is resolved for measurement purposes by reimaging the photons and measuring them only at the image plane, where the relative phase difference disappears.

Plotted on the two-dimensional LG mode OAM Bloch sphere analog of Figure 2.6 are the MUBs for $\ell_j = 1$, $\ell_k = -1$, which exist along the Cartesian axes. The two-dimensional qubit basis b_2 chosen by the unitary operator of Equation (2.4) is seen at the poles of the x-axis. Shown in Figure 2.7a, the b_2-basis qubits $(|0\rangle_{M_j}, |1\rangle_{M_j})$ for $\ell_j, \ell_k = \{\pm1, \pm2, \pm3, \pm4\}$ can be plotted similarly on the Bloch sphere. Notice that for higher-order modes, the number of intensity lobes in a $360°$ ring depends on $2k_j = 2|\ell|$. These are referred to as petal modes because of the petal-like patterns they form.

In Figure 2.7b, the initial state of the QFA, given by Equation (2.6), is a superposition of the top row of basis states $(|0\rangle_{M_j})$. As the structure rotates, the overlap squared of the final state with the initial state, or accepting probability, evolves as shown in Figures 2.4a and 2.4b (for $\mathfrak{p} = 11$).

Recall from Equation (2.9) that once the MUB b_2 is chosen, the QFA operations evolve the qubit state structure depending on the rotational operator R_{k_j} of Equation (2.7), which depends on $\phi_{k_j} = k_j\ 2\pi/\mathfrak{p}$. As detailed in the Methods section (Chapter 3), the angle $2\pi/\mathfrak{p}$ is a physical rotation of the state structure (reading a character of the input string) realized experimentally by passing the photon through a Dove prism. The angle 2π can be replaced by any final angle, such as $\pi/2$ or π, as will be shown in the Results section (Chapter 4).

It is worth noting that it is possible to use other photonic degrees of freedom, such as polarization, to encode qubit states, but the state space utilized here has infinite spatial dimensions, while the polarization state space is limited to 2 dimensions (horizontal and vertical and superpositions thereof) [10]. To perform multi-qubit calculations with polarization states, one needs to encode the information across multiple photons in a joint

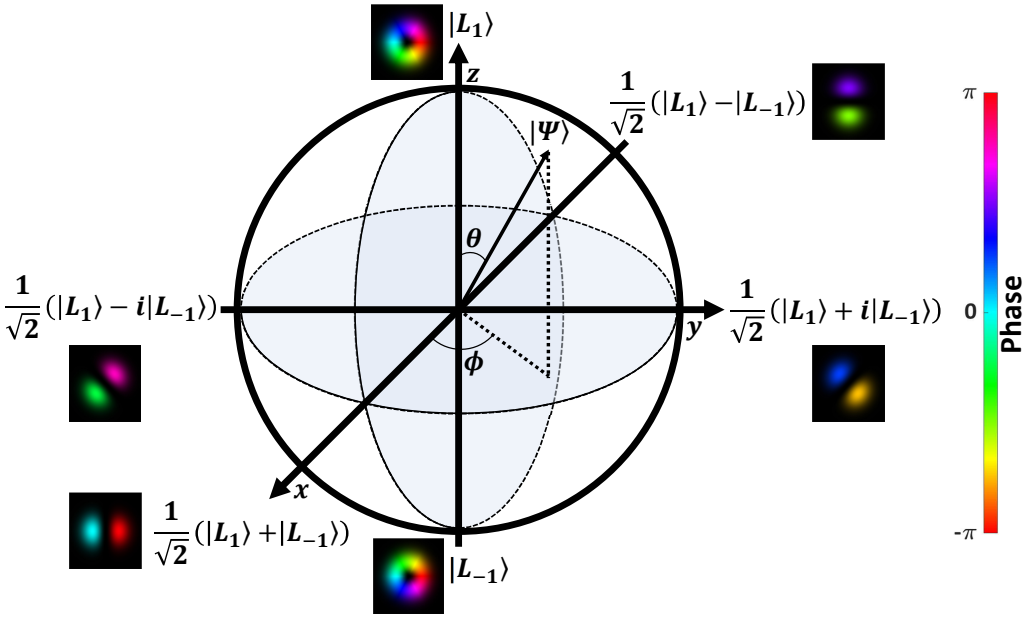

Figure 2.6 Bloch sphere analog of LG-mode OAM qubits in two-dimensional Hilbert space with $\ell = \pm 1$. The color spectrum represents the azimuthal phase $\delta = \ell\theta_r$ from $-\pi$ to π, with the brightness representing the probability density (intensity). Recall that the structure pairs at the poles of each Cartesian axis form a set of MUBs, as in Equation (2.2).

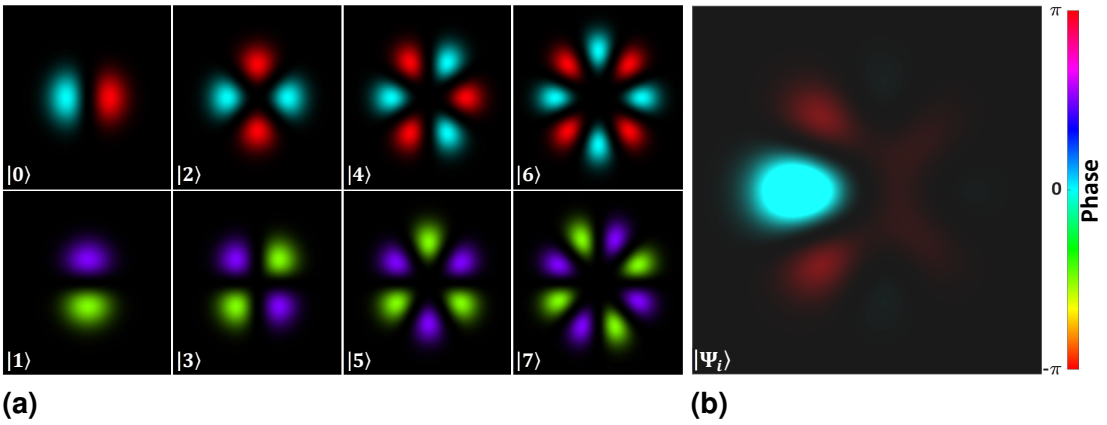

Figure 2.7 **(a)** Qubit basis states for $\{k_1, k_2, k_3, k_4\} = \{1, 2, 3, 4\}$. **(b)** The initial state of the four-qubit QFA system, given by $|\Psi_i\rangle = (|0\rangle + |2\rangle + |4\rangle + |6\rangle)/2$. Note that the image in **(b)** has been brightened to emphasize the state structure, with some saturation of the intensity (probability distribution) as a result.

coherent (entangled) state, while here the multi-qubit state is encoded on a single photon.

With the theoretical understanding outlined above, the experimental methodology used to realize a multi-qubit QFA using structured photons will now be described. After all, "only questions about the results of experiments have a real significance and it is only such questions that theoretical physics has to consider" [7].

3 METHODS

This chapter details the methods used to realize a photonic QFA of up to four qubits. The experimental setup includes a Type II spontaneous parametric down-conversion (SPDC) heralded single photon source; a spatial light modulator (SLM) to generate the qubits and measure the final state; a beamsplitter loop and Dove prism to act as a QFA reading an input string by imparting successive rotational operations R_{k_j} on the photons; and two single-photon detectors with accompanying hardware and software for the coincidence logic (time tagging).

3.1 Experimental design

Shown in a simplified diagram in Figure 3.1 is the optical setup used to realize the QFA.

The Type II SPDC source consists of a periodically-poled potassium titanyl phosphate (ppKTP) crystal (RAICOL Crystals Ltd., $1\times2\times5$ mm^3, poling period ~10 μm) pumped by a laser diode (Toptica iBeam SMART-405-S-HP) emitting photons at 405 nm, which split with low probability into signal (herald) and idler (qubit) photon pairs with orthogonal polarizations at 810 nm, as detailed in Section 3.1.1. The polarizing beamsplitter (PBS) splits the signal from the idler. The signal photon is coupled into a single-mode fiber (SMF) and counted at Detector 1 (Laser Components Count-T100-FC) with a time tagger (ID Quantique's ID900 Time Controller), where the time delay between it and its idler mate can be measured. The idler is coupled into an SMF that leads to the qubit arm.

After outcoupling to the qubit path, it is encoded with a single- or multi-qubit structure by a holographic pattern on the SLM, as explained in Section 3.1.2.1. The structured photon passes through a 1:3 demagnification 4f lens system, and an iris at the Fourier plane selects the first diffraction order, where the holographic beam shaping is most efficient. It passes through a beamsplitter. On the throughpath, it is rotated by a Dove prism at the reimaging plane (see Section 3.1.2.2). After $\mathfrak{n} \in \{0, 1, 2, ...\}$ rotations, the photon enters the reflected beam path with a probability dependent on the type of beamsplitter used. For a 50:50 beamsplitter, the probability is $P^B_{\mathfrak{n}} = 1/2^{\mathfrak{n}+1}$. With a general R:T beamsplitter, a photon has a $R\%$ chance to be reflected without being rotated. For $\mathfrak{n} \geq 1$, the probability for the photon to leave the loop is governed by the equation $P^B_{\mathfrak{n}} = t^2(r^{\mathfrak{n}-1})$, where r and t are the reflection and transmission coefficients, given by $r = R/100$ and $t = T/100$, respectively.

A photon on the reflected beam path is remagnified in a 3:1 4f system and measured,

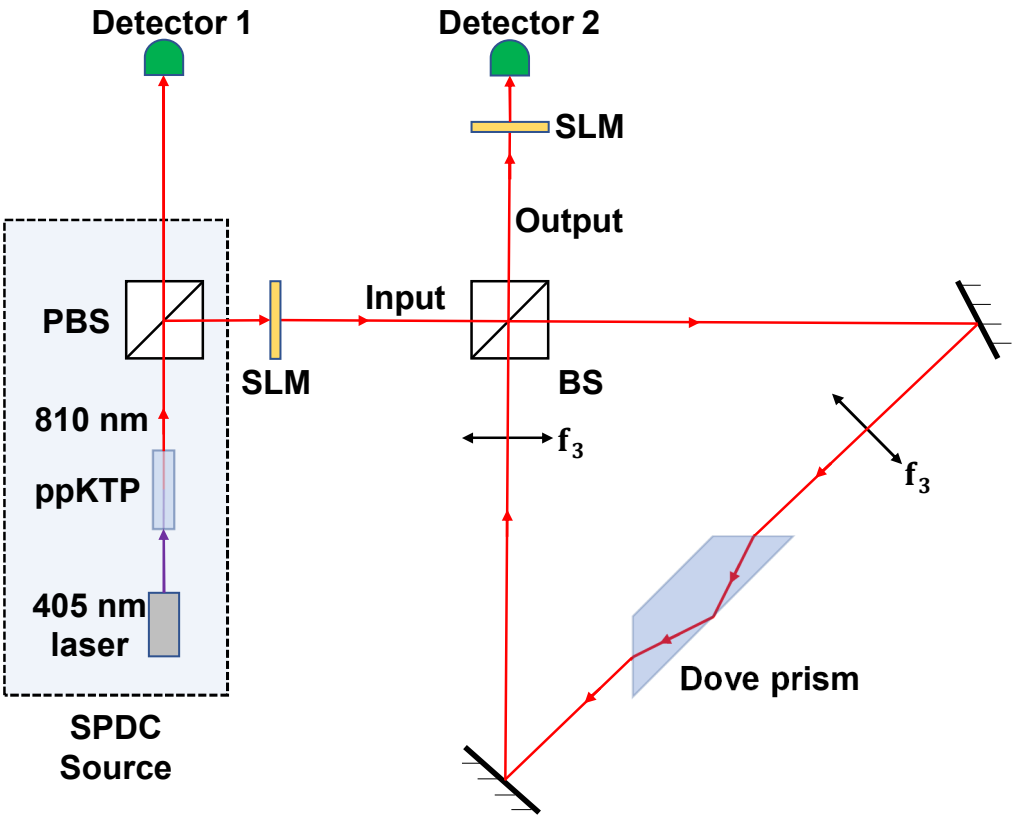

Figure 3.1 A simplified experimental setup (not to scale) of the Type II SPDC source, the heralding arm, and the qubit arm. The PBS separates the Type II pairs, directing one to heralding Detector 1 and its orthogonally-polarized mate to the qubit arm, where an SLM encodes its initial state. A beamsplitter loop accepts the photon $\mathfrak{n}$ times with a probability dependent on the BS's reflection and transmission coefficients, and a Dove prism centered at the image plane of the rightmost lens $f_3 = 150$ mm rotates the structure $\mathfrak{n}$ times. A photon on the reflected beam path is phase-flattened at the 2^{nd} SLM and outcoupled to Detector 2 with accepting probability $0 \leq |\langle \Psi_f | \Psi_i \rangle|^2 \leq 1$.

as described in Section 3.2.

3.1.1 Heralded single photons (Type II SPDC)

An experimental realization of simultaneous photon pair production via SPDC was first demonstrated in [6], and a later experiment demonstrated the existence of nearly-ideal localized single-photon states [12]. Two detectors measure single-photon rates, and coincidence counts verify the presence of signal and idler pairs above the background noise. The signal photon is said to herald the presence of its idler mate.

This experiment uses the source shown in Figure 3.2a, which consists of a 405 nm pump beam outcoupled via an SMF to the beam path, then collimated with a 75 mm lens and focused with a 100 mm lens to a beam waist of $w_0 \approx 26.4$ μm in the center of a

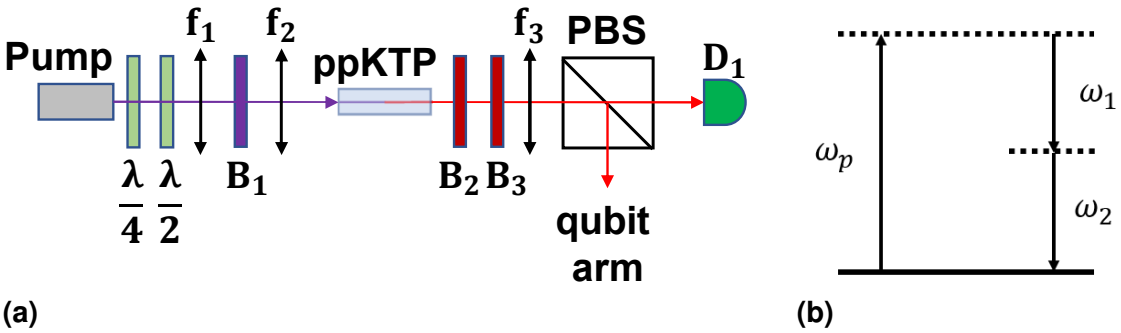

Figure 3.2 SPDC. **(a)** Type II SPDC photon source (not to scale). The optical elements include a 405 nm pump laser; a quarter-wave plate $\lambda/4$ for 405 nm; a half-wave plate $\lambda/2$ for 405 nm; a fused silica (FS) collimating lens $f_1 = 75$ mm; a 405 nm ± 10 nm band pass filter (BPF) B_1; an FS focusing lens $f_2 = 100$ mm; a ppKTP crystal; an 810 nm ± 10 nm BPF B_2; an 810 nm ± 3 nm BPF B_3; and an N-BK7 collimating lens $f_3 = 150$ mm. The PBS separates the Type II pairs, which are coupled via $\times 10$ microscope objectives and SMFs to the heralding arm detector D_1 and the qubit arm. **(b)** A photon diagram that shows the SPDC process that occurs in the ppKTP crystal.

ppKTP crystal housed in a temperature-tunable oven. The crystal has a large second-order susceptibility χ^2 that leads to a nonlinear response that generates photon pairs with orthogonal polarizations in a three-wave mixing process known as Type II SPDC, represented by the photon diagram of Figure 3.2b.

The nonlinear response depends on the polarization of the pump field, so a quarter-wave plate and a half-wave plate are used to control the output photon rate. The process is governed by energy and momentum conservation such that the frequency ω_p (wave vector $\mathbf{k}_p$) of a pump photon is equal to the sum of the frequencies ω_i (wave vectors $\mathbf{k}_i$) of the photon pair,

$$\omega_p = \omega_1 + \omega_2 \;\; ; \;\; \mathbf{k}_p = \mathbf{k}_1 + \mathbf{k}_2, \tag{3.1}$$

which are also known as phase-matching conditions. While perfect phase matching is impractical, quasi-phase-matching conditions can be achieved through a variety of techniques involving the application of a periodically inverted electric field to the ferroelectric crystal, thus forming periodic domains of opposite polarizations. The quasi-phase-matching condition is then

$$\mathbf{k}_p(\lambda_p, n_p(\lambda_p, T)) = \mathbf{k}_1(\lambda_1, n_1(\lambda_1, T)) + \mathbf{k}_2(\lambda_2, n_2(\lambda_2, T)) + \frac{2\pi}{\Lambda(T)}, \tag{3.2}$$

where $\mathbf{k}_p$ and $\mathbf{k}_i$ depend on the wavelengths of the pump and generated photons (λ_p, λ_i) and the refractive indices of the crystal (n_p, n_i). The indices depend on both wavelength and temperature [10]. The third term includes the poling period Λ, whose temperature dependence means that increasing or decreasing the temperature lengthens or shrinks the size of the poled regions, thus changing the phase-matching conditions and resulting out-

put wavelengths λ_i and wave vectors $\mathbf{k}_i$.

For this experiment, degenerate photons are desired with matching wavelengths at $\lambda_i = 810$ nm and co-linear wave vectors. The crystal used was therefore manufactured with properties that enable these conditions. The optimal operating temperature for degeneracy, unique to this crystal, was found to be $23.5°$ C by varying the oven temperature and observing the spectrum, coincidence counts, and wavefront of the photons. When the spectra of each beam past the PBS were centered at ~810 nm, maximum pair production was ensured. The wavefront image was taken by a high-sensitivity, temperature-controlled camera to ensure a Gaussian profile, which appears for wave vector overlap but has non-Gaussian curvature at other temperatures.

After down-conversion, the beam diverges to a beam radius of $w \approx 1500$ μm and is collimated at a 150 mm lens placed before the PBS, which separates photon pairs that are then coupled via $\times 10$ microscope objectives into SMFs that lead to the heralding detector and the qubit arm.

3.1.2 The qubit arm

As shown in Figure 3.3, the qubit arm of the experiment consists of an SLM; a $1{:}3$ 4f demagnification and diffraction order filtering system; a beamsplitter loop and Dove prism (rotational operator); and a $3{:}1$ remagnification system.

An idler photon coupled into the qubit arm via an SMF from the source passes through a quarter-wave plate that cleans its polarization state, $\vec{P}$, by removing any ellipticity introduced indeterminately by the fiber. The idler then passes through a half-wave plate that aligns $\vec{P}$ such that the operating efficiency of the SLM is maximized when it encodes the photon with its initial state $|\Psi_i\rangle$, a process described in Section 3.1.2.1. The structured photon then encounters the beamsplitter loop and Dove prism, which performs the QFA's unitary rotation operations, as detailed in Section 3.1.2.2. A photon on the reflected beam path has its structure measured in a procedure described in Section 3.2.

3.1.2.1 Structuring the light

As shown in Figure 3.4, a photon in the qubit arm has a state structure $|\Psi_i\rangle$ encoded on it by a hologram on the screen of a Holoeye PLUTO-2.1-NIR-015 twisted nematic liquid crystal on silicon (LCOS) phase-only spatial light modulator (SLM) calibrated for use at 810 nm. The SLM operates via pixel-resolution voltage control of the orientation of the birefringent liquid crystals (LCs) in the display, which determines how the phase of the transverse structure is modulated [24]. This holographic modulation process is ~70%

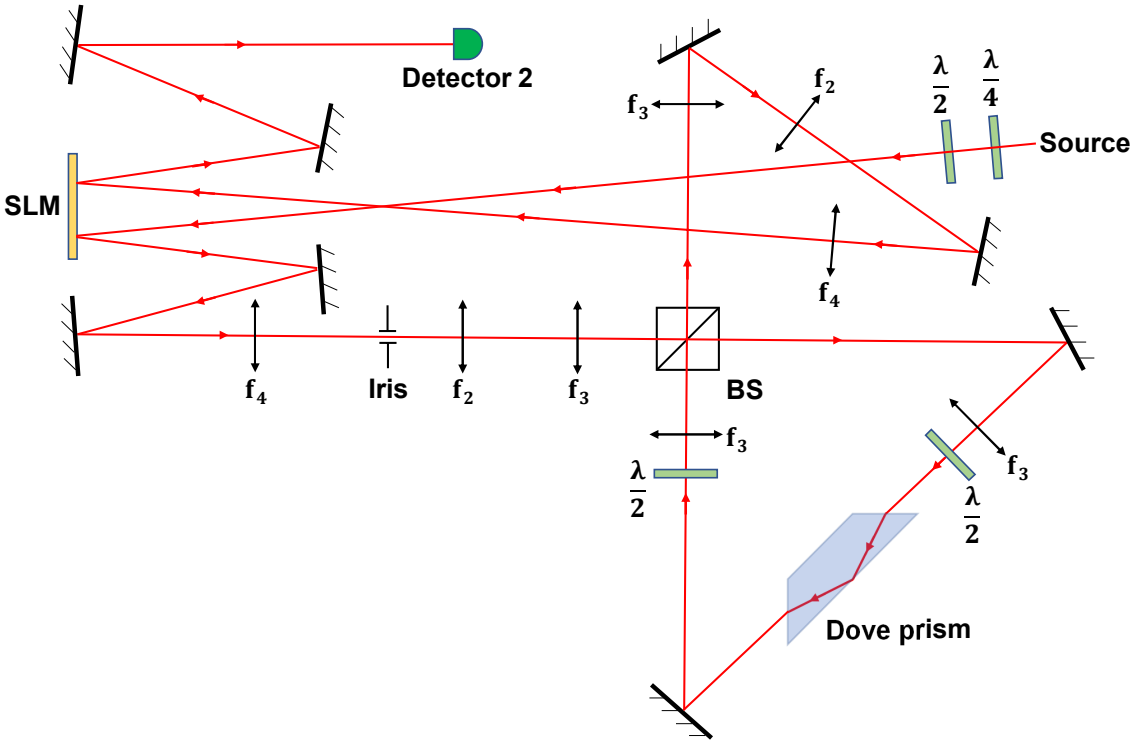

Figure 3.3 The qubit arm (not to scale). After the SPDC source, there are a quarter-wave plate $\lambda/4$ for 810 nm; a half-wave plate $\lambda/2$ for 810 nm; an SLM (right half of screen); a focusing lens $f_4 = 300$ mm; an iris to filter the first diffraction order; a collimating lens $f_2 = 100$ mm; a focusing lens $f_3 = 150$ mm; a beamsplitter loop; and a reflected beam path. The beamsplitter loop has a collimating lens f_3; a half-wave plate $\lambda/2$ for 810 nm; a Dove prism centered at the image plane of collimating lens f_3; a half-wave plate $\lambda/2$ for 810 nm; and a focusing lens f_3. The reflected beam path has a collimating lens f_3; a focusing lens f_2; a collimating lens f_4; an SLM (left half of screen); and a $\times 10$ microscope objective that couples the photons into an SMF that leads to Detector 2.

efficient[1] to the first diffraction order of the 4f system when the linear polarization state of the photon is optimized with respect to the orientation of the (fixed) top layer of LCs in the SLM [10]. To encode the state structure, a phase pattern carrying the qubit-state information is overlaid on the grating, while the amplitude is modulated using the carving technique detailed in [5].

3.1.2.2 Looping the photon (QFA operations)

A photon on the throughpath of the beamsplitter loop is reimaged at the Dove prism, whose effect on the photon's path is shown in Figure 3.5, with the corresponding ABCD

[1] measured by displaying a vertical diffraction grating on the SLM, which reflected the modulated photons to the first and higher diffraction orders, while the unmodulated photons were reflected to the zeroth order.

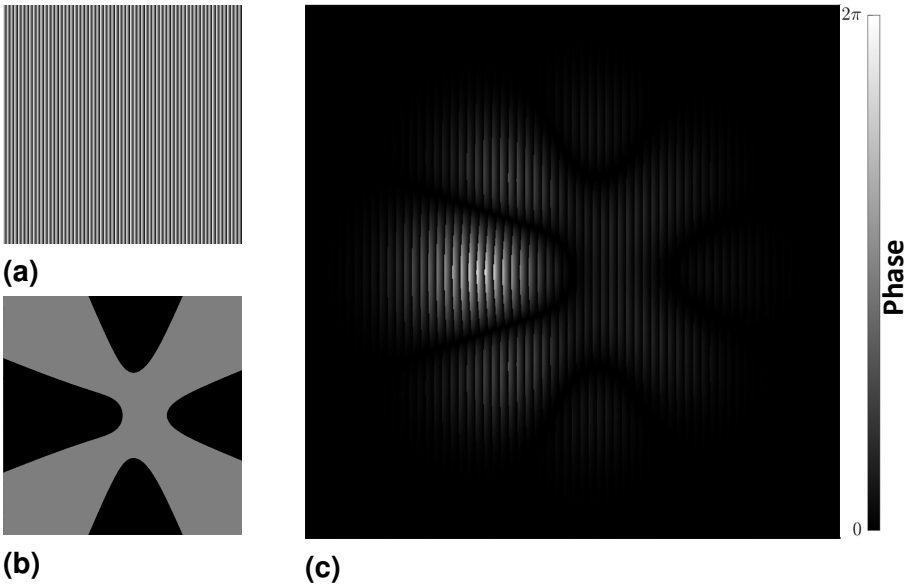

Figure 3.4 SLM screen patterns for generation. **(a)** A vertical diffraction grating enables filtering of the modulated photons by the iris to the first diffraction order. **(b)** A phase pattern of the four-qubit superposition of Equation (2.6). **(c)** The photon structure matching that of the four-qubit QFA state simulated in Figure 2.7b, formed by combining **(a)** and **(b)** with the amplitude carving technique in [5].

matrices for a Dove prism in the paraxial approximation given in Equations (3.3) and (3.4) [11]:

$$\begin{pmatrix} x_2 \\ o_x \end{pmatrix} = \begin{pmatrix} 1 & [\frac{L}{n} + \frac{h_0}{tan(\alpha)}(1 - \frac{1}{n})] \\ 0 & 1 \end{pmatrix} \begin{pmatrix} x_1 \\ i_x \end{pmatrix} \tag{3.3}$$

$$\begin{pmatrix} y_2 \\ o_y \end{pmatrix} = \begin{pmatrix} \frac{h_0}{y_1} - 1 & -h_0(\frac{\eta}{n} + \frac{1}{tan(\alpha)}) \\ 0 & -1 \end{pmatrix} \begin{pmatrix} y_1 \\ i_y \end{pmatrix}, \tag{3.4}$$

where L is the length of the base of the Dove prism, n is the refractive index (here of N-BK7, a borosilicate glass), and α is the base angle (here $45°$). The input angles and positions are (i_x, i_y) and (x_1, y_1), with the output angles and positions (o_x, o_y) and (x_2, y_2). It is important to align the prism to minimize the angles $(i_y, o_y, i_x, i'_x, o_x)$ such that two conditions are met: a photon on its first loop has the same path as a photon on its second or higher loops, and a photon on the reflected beam path after $\mathfrak{n} = \{0, 1, 2, ...\}$ loops has the same path for all $\mathfrak{n}$. In other words, the goal is to have $(x_1, y_1) = (x_2, y_2)$. The ideal photon path is shown by a dashed line in Figure 3.5, achieved by aligning the setup without the prism using an 810 nm laser, then placing the prism in and adjusting its position

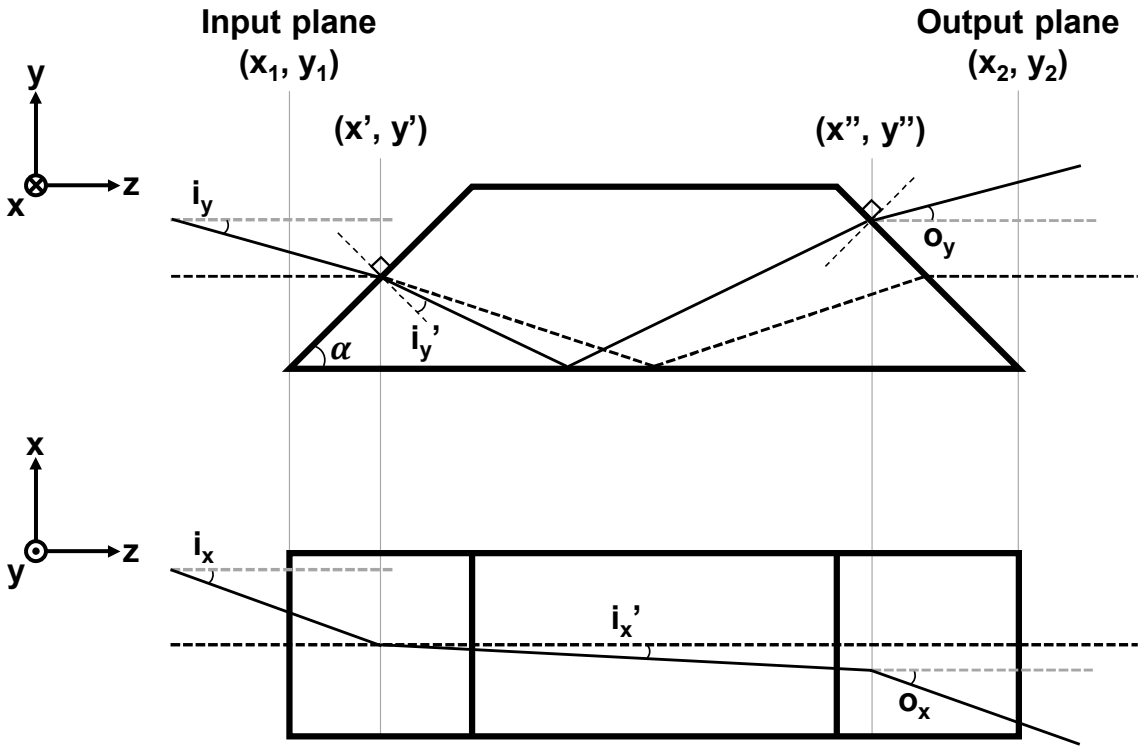

Figure 3.5 Dove prism diagram with input and output positions and angles. The z-axis is the same as the propagation axis of the optical system.

such that the beam path again overlaps from the beamsplitter to the final outcoupler.

As depicted in Figure 3.6, rotating the Dove prism by an angle β with respect to the x-axis causes a rotation of the transverse structure of the light by 2β. After changing the prism angle, the beam path must be realigned from the beamsplitter to the final outcoupler.

Because Dove prisms cause amplitude modulation in polarized light dependent on their rotation angle relative to $\vec{P}$, and the Dove prism has no effect on the amplitude of light with polarization parallel to or perpendicular to its input plane [16], a half-wave plate is placed before the prism to rotate $\vec{P}$ such that the transmission of the prism is maximized. A second half-wave plate is placed after the prism, before the beamsplitter, to return the photons to the same polarization as the photons on the incident and reflected beam paths.

The path length of the beamsplitter loop, determined by the reimaging lenses, ensures a timelike path length between photons leaving the loop greater than the time-resolution of the detector (500 ps): 15 cm lenses, for a nominal path length of 60 cm, delay successive rotations by approximately 2 ns ($\Delta x = c \cdot t$). The Dove prism is a large block of glass that, by the Pythagorean theorem and its refractive index ($n_{N-BK7} = 1.5106$ at 810 nm), introduces an effective optical path length that was observed during alignment to cause different magnifications in the size of the reimaged laser beam in successive loops: the $\mathfrak{n} = 1$ beam was smaller than the $\mathfrak{n} = 0$ beam, and the $\mathfrak{n} = 2$ beam was larger. This effect was compensated for experimentally by moving the second mirror to increase the

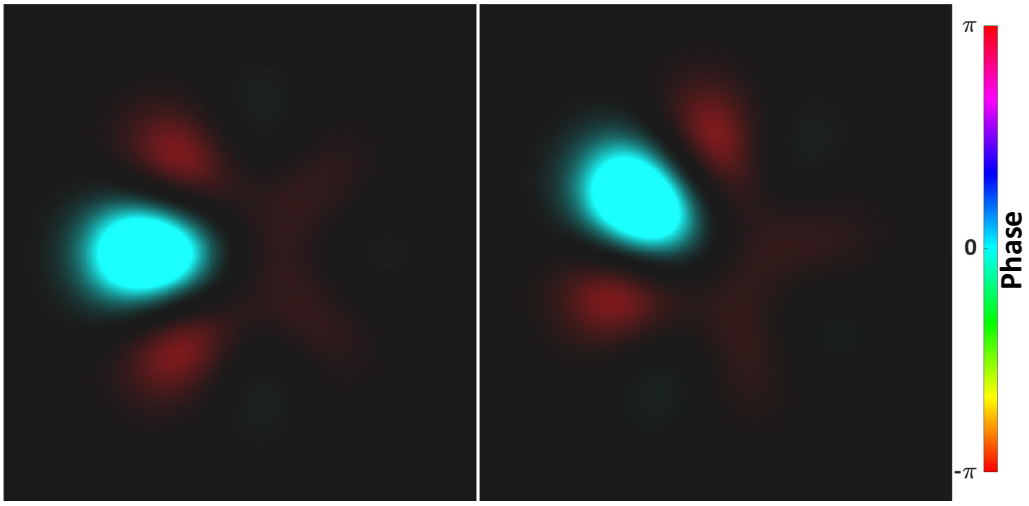

Figure 3.6 Simulated rotation of the transverse structure by $2\beta = 360°/11 \approx 32.7°$.

distance between the lenses in the loop and using a camera to ensure each loop's structure overlapped after the $3{:}1$ remagnification system. The triangular length of the loop, as measured with a ruler, was then about 62 cm.

As shown in Figure 3.3, a remagnified photon reflects off the left half of the SLM screen. Its state is measured in a process described below.

3.2 Measurement

A photon hitting the SLM screen encounters the holographic pattern shown in Figure 3.7, which is designed to flatten the phase structure generated by the mask in Figure 3.4. If the photon's structure aligns with the pattern on the screen, then it returns to a near-Gaussian structure and is coupled into the SMF leading to Detector 2, corresponding to a nominal accepting probability of $|\langle\Psi_f|\Psi_i\rangle|^2 = 1$. If the photon has been rotated such that its structure does not align with the pattern on the mask, then its accepting probability varies as predicted by Figure 2.4a.

The process of phase flattening by the SLM and mode filtering with the SMF corresponds to the measurement in the computational basis described in the paragraph after Equation (2.9): if all four qubits are in states orthogonal to their initial states, then the phase-flattening fails and the state (string) is rejected because the photon does not couple into the SMF. If the qubit states have nonzero probabilities to be projected onto the accepting state, then there is some decision error, meaning the wavefront has some Gaussian components that cause photons to couple into the SMF with probabilities between 0 and 1.

Coupling data were collected by recording time-domain histograms of coincidence counts between the heralding arm (Detector 1) and the qubit arm (Detector 2). Because

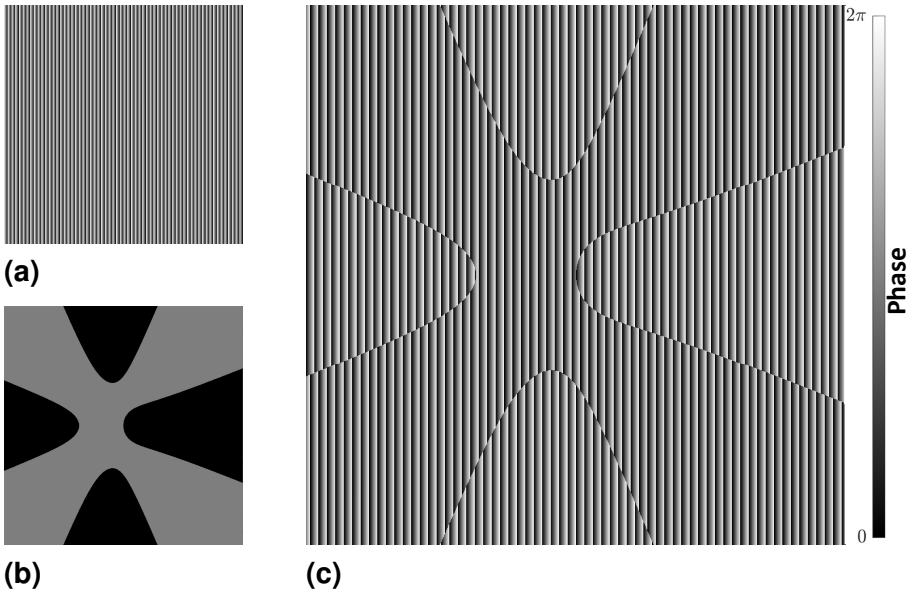

Figure 3.7 SLM screen patterns for measurement. **(a)** A vertical diffraction grating. **(b)** A phase pattern of the four-qubit superposition of Equation (2.6), flipped to account for the mirrors and Fourier planes of the setup. **(c)** The mask used to measure the state by phase-flattening the wavefront generated by the pattern in Figure 3.4c. Amplitude carving is unnecessary for measurement.

of the mode filtering measurement technique, qubit-mode coincidence counts were normalized to Gaussian-mode coincidence counts, as shown in the next chapter.

4 RESULTS

In this chapter we present the results of our efforts to "wring significant facts from an inflexible Nature, who says so distinctly 'No' and so indistinctly 'Yes' to our theories" [23]. The results demonstrate that single photons structured in the high-dimensional state space of LG modes can feasibly be used as multi-qubit QFAs.

4.1 Data

The data include single- and multi-qubit coincidence counts obtained as time-domain histograms from the QFA experiment described in Chapter 3 with the Dove prism at three different orientations. Due to experimental losses and inefficiencies, especially the efficiency of the SPDC source (a coincidences to singles ratio of about 13%), the highest resolvable loop number in the coincidence histograms was $\mathfrak{n} = 5$, so the prime number $\mathfrak{p} = 5$ was analyzed.

In three separate experiments, the Dove prism was oriented at angles of $\beta_1 = 9° \pm 0.5°$, $\beta_2 = 18° \pm 0.5°$, and $\beta_3 = 36° \pm 0.5°$, which rotated the state structure by $2\beta_j$ per loop, for final angles after $\mathfrak{n} = 5$ loops of $\phi_j = 10\beta_j$. The uncertainty in angle increases linearly with each loop, described by $\Delta\phi'_{\mathfrak{n}} = 0.5° \pm (0.5° \cdot \mathfrak{n})$. The final angles were therefore $\phi_1 = 90° \pm 3.0°$, $\phi_2 = 180° \pm 3.0°$, and $\phi_3 = 360° \pm 3.0°$, respectively.

Histogram data were collected for each angle for single-qubit modes with $\ell = \{\pm 1, \pm 2, \pm 3, \pm 4, \pm 5\}$; double-qubit modes with ($\ell_1 = \pm 1,\ \ell_2 = \pm 2$), ($\ell_1 = \pm 1$, $\ell_2 = \pm 3$), and ($\ell_1 = \pm 2,\ \ell_2 = \pm 4$); triple-qubit modes with ($\ell_1 = \pm 1,\ \ell_2 = \pm 2,\ \ell_3 = \pm 3$), and ($\ell_1 = \pm 1,\ \ell_2 = \pm 3,\ \ell_3 = \pm 5$); and the four-qubit mode with ($\ell_1 = \pm 1,\ \ell_2 = \pm 2,\ \ell_3 = \pm 3,\ \ell_4 = \pm 4$). The bin width was 100 ps, and acquisition times varied from 10 s for the Gaussian mode to 30 s, 60 s, 120 s, or 180 s for single- or multi-qubit modes. Longer collection times ensured adequate photon counts when much of the light was removed by the amplitude-carved masks, and at least $\mathcal{N} = 10$ data runs were completed for each state. The delay time on Detector 1 was set to $44,200$ ps to account for the length of the qubit arm.

The histogram data in Figure 4.1 were collected with the Dove prism at $\beta_3 = 36° \pm 0.5°$, for a final angle after $\mathfrak{n} = 5$ loops of $\phi_3 = 360° \pm 3.0°$. In Figure 4.1a are data for an amplitude-carved Gaussian mode, and in Figure 4.1b are corresponding data for the four-qubit mode of Equation (2.9) with $\{k_1, k_2, k_3, k_4\} = \{1, 2, 3, 4\}$, which is pictured in Figure 2.7b, generated with the SLM hologram of Figure 3.4, and measured with the SLM

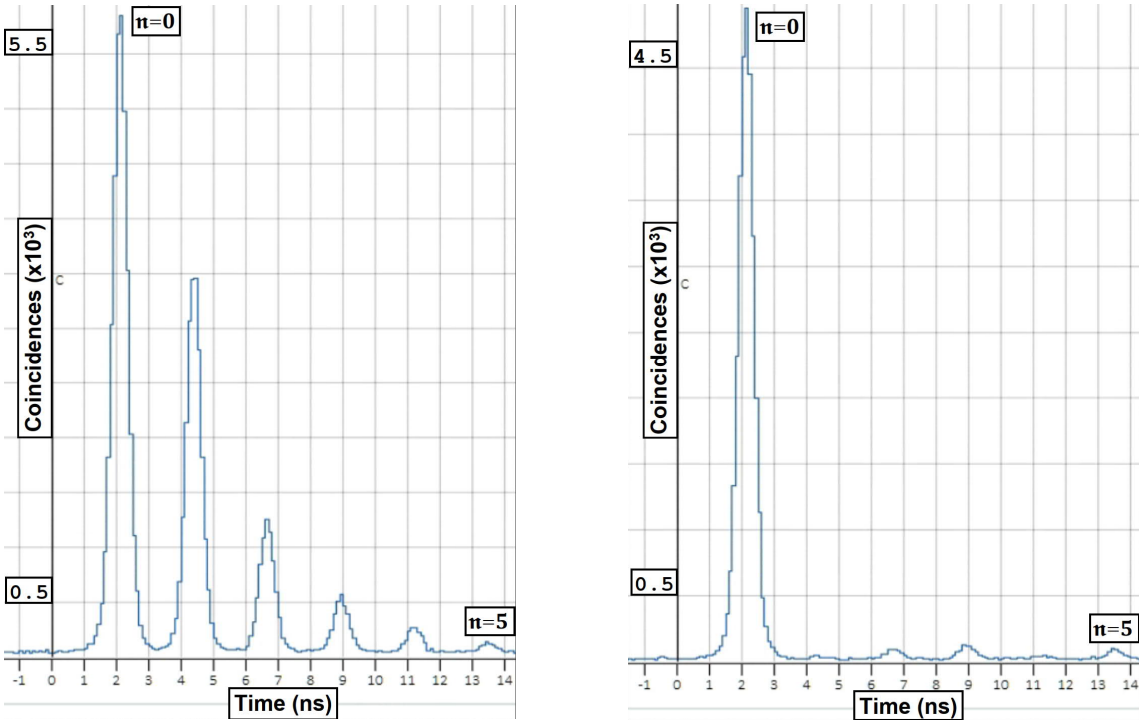

Figure 4.1 Coincidence histograms. **(a)** Gaussian mode histogram. **(b)** Four-qubit mode histogram. Note that these are screenshots taken during acquisition, and thus are not representative of final counts.

hologram of Figure 3.7. Note that the height of the peak where $\mathfrak{n} = 5$ is similar in each histogram, showing that the qubit mode has been phase-flattened by the measurement mask and efficiently coupled into the SMF.

Away from the peaks, the counts do not reach zero due to accidental coincidence counts caused by background noise, the sources of which are (rarely) stray photons in the dark lab and (mainly) single 810 nm photons (without SPDC mates) generated in linear processes in the ppKTP crystal. The accidentals are proportional to the product of the single counts at each detector times the bin width; they are accounted for in the analysis, described in the next section.

4.1.1 Analysis

The analysis process involved defining a 10-bin, 1 ns coincidence window around the maximum of the peak of each loop; summing the coincidences, $C_{\mathfrak{n}}$, within the window; subtracting the average accidentals per bin, $\overline{A}$; and normalizing them to obtain a coupling (accepting) probability, $P_{\mathfrak{n}}$. The counts per loop, $C_{\mathfrak{n}}$, are described:

$$C_{\mathfrak{n}} = \sum_{b=1}^{b=10} (C_b - \overline{A}), \tag{4.1}$$

where b refers to the bin number.

The Gaussian counts, $C_{\mathfrak{n}}^G$, were normalized such that the sum of the $\mathfrak{n} = 0$ peak was set to 1:

$$P_{\mathfrak{n}}^G = \frac{C_0^G}{C_{\mathfrak{n}}^G}. \tag{4.2}$$

The mean probability, $\overline{P}_{\mathfrak{n}}^G$, was averaged over $P_{\mathfrak{n}}^G$ from $\mathcal{N}$ collection runs, and the standard deviation, $\sigma_{\mathfrak{n}}^G$, was taken.

The qubit-mode counts, $C_{\mathfrak{n}}^M$, were first normalized and averaged in the same manner, then renormalized to the Gaussian probabilities:

$$P_{\mathfrak{n}}^M = \frac{C_0^M}{C_{\mathfrak{n}}^M}; \;\; P_{\mathfrak{n}} = \frac{\overline{P}_{\mathfrak{n}}^M}{\overline{P}_{\mathfrak{n}}^G} = \frac{M}{G}, \tag{4.3}$$

The propagation of uncertainty was accounted for:

$$\sigma_{\mathfrak{n}} = \sqrt{\left(\frac{\partial P_{\mathfrak{n}}}{\partial_M}\right)^2 \cdot \sigma_{\mathfrak{n}}^{M\,2} + \left(\frac{\partial P_{\mathfrak{n}}}{\partial_G}\right)^2 \cdot \sigma_{\mathfrak{n}}^{G\,2}}. \tag{4.4}$$

With this analysis process, the accepting probabilities of Figures 4.2, 4.3, 4.4, and 4.5 were found for one-, two-, three-, and four-qubit modes, respectively. The experimental data of the N-qubit QFA system were compared to theoretical expectations by rewriting Equations (2.5), (2.6), and (2.9) for N qubits, as described here.

A general N-qubit state is an equally-weighted superposition of qubit vectors:

$$|\Psi\rangle = \frac{1}{\sqrt{N}} \begin{pmatrix} \cos(\theta_1/2) \\ -i\,\sin(\theta_1/2) \\ \hline \cos(\theta_2/2) \\ -i\,\sin(\theta_2/2) \\ \hline \cdots \\ \cdots \\ \hline \cos(\theta_{N-1}/2) \\ -i\,\sin(\theta_{N-1}/2) \\ \hline \cos(\theta_N/2) \\ -i\,\sin(\theta_N/2) \end{pmatrix}. \tag{4.5}$$

The initial state of the QFA system of N qubits is:

$$|\Psi_i\rangle = \frac{1}{\sqrt{N}} \begin{pmatrix} 1 \\ 0 \\ \hline 1^2 \\ 0 \\ \hline ... \\ ... \\ \hline 1^{N-1} \\ 0 \\ \hline 1^N \\ 0 \end{pmatrix}. \tag{4.6}$$

The final state of the QFA system, for some final angle ϕ_j, is:

$$|\Psi_f\rangle = \frac{1}{\sqrt{N}} \begin{pmatrix} \cos(\mathfrak{n}k_1 \frac{\phi_j}{\mathfrak{p}}) \\ -i \sin(\mathfrak{n}k_1 \frac{\phi_j}{\mathfrak{p}}) \\ \hline \cos(\mathfrak{n}k_2 \frac{\phi_j}{\mathfrak{p}}) \\ -i \sin(\mathfrak{n}k_2 \frac{\phi_j}{\mathfrak{p}}) \\ \hline ... \\ ... \\ \hline \cos(\mathfrak{n}k_{N-1} \frac{\phi_j}{\mathfrak{p}}) \\ -i \sin(\mathfrak{n}k_{N-1} \frac{\phi_j}{\mathfrak{p}}) \\ \hline \cos(\mathfrak{n}k_N \frac{\phi_j}{\mathfrak{p}}) \\ -i \sin(\mathfrak{n}k_N \frac{\phi_j}{\mathfrak{p}}) \end{pmatrix}. \tag{4.7}$$

The square of the overlap between the final state and the initial state (accepting probability) can be calculated:

$$|\langle \Psi_f | \Psi_i \rangle|^2 = \left(\frac{1}{\sqrt{N}} \right)^2 \left(\sum_{N=1}^{N} \cos(\mathfrak{n}k_N \frac{\phi_j}{\mathfrak{p}}) \right)^2, \tag{4.8}$$

where the $i \sin(\mathfrak{n}k_N \frac{\phi_j}{\mathfrak{p}})$ terms drop out of the inner product because they are multiplied by the 0's of the initial state vector, $|\Psi_i\rangle$, of Equation (4.6).

It is Equation (4.8) that generated the theoretical curves in Figures 4.2, 4.3, 4.4, and 4.5. One can see that measurements tend to agree with the predicted sinusoidal curves,

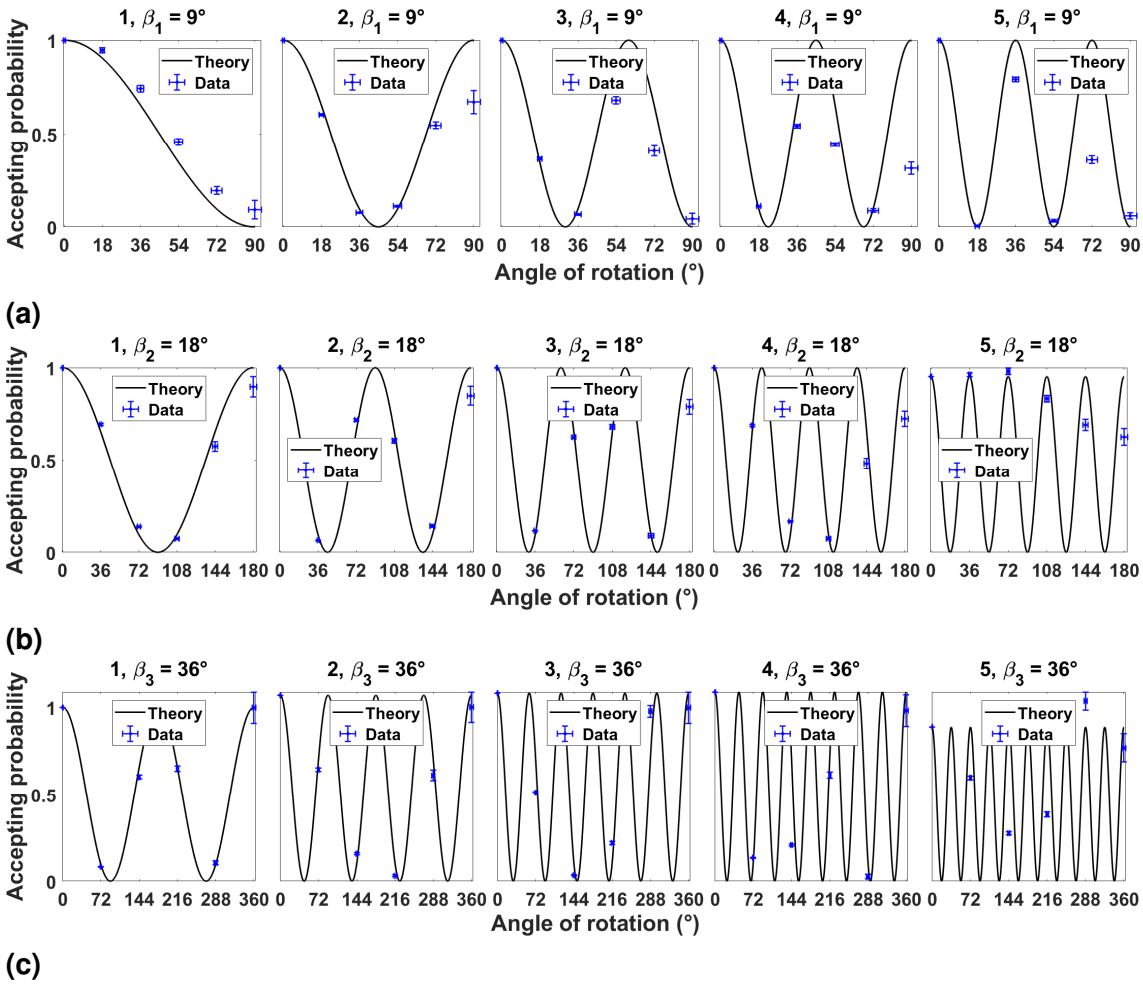

Figure 4.2 Single-qubit measurements for petal modes $\ell = \{\pm1, \pm2, \pm3, \pm4, \pm5\}$ with the Dove prism at **(a)** $\beta_1 = 9° \pm 0.5°$, **(b)** $\beta_2 = 18° \pm 0.5°$, and **(c)** $\beta_3 = 36° \pm 0.5°$.

with noticeable outliers explainable by experimental errors and inefficiencies, as discussed in Section 4.1.1.1.

4.1.1.1 Losses and errors

This section discusses the effects of systemic losses and experimental errors.

The loss per loop was measured with the alignment laser and a power meter to be 6.67%, caused by the absorption or scattering of photons by the optical components of the beamsplitter loop. This made it necessary to measure for a longer time, compared to a system with less or zero loss, to get adequate counts for higher $\mathfrak{n}$, so the stability of the optical setup was essential.

The main factors contributing to the experimental error were the precision of the angle of rotation of the Dove prism and the alignment of the beam paths of successive loops.

The Dove prism was first oriented using a digital caliper at its reference axis of $\beta =$

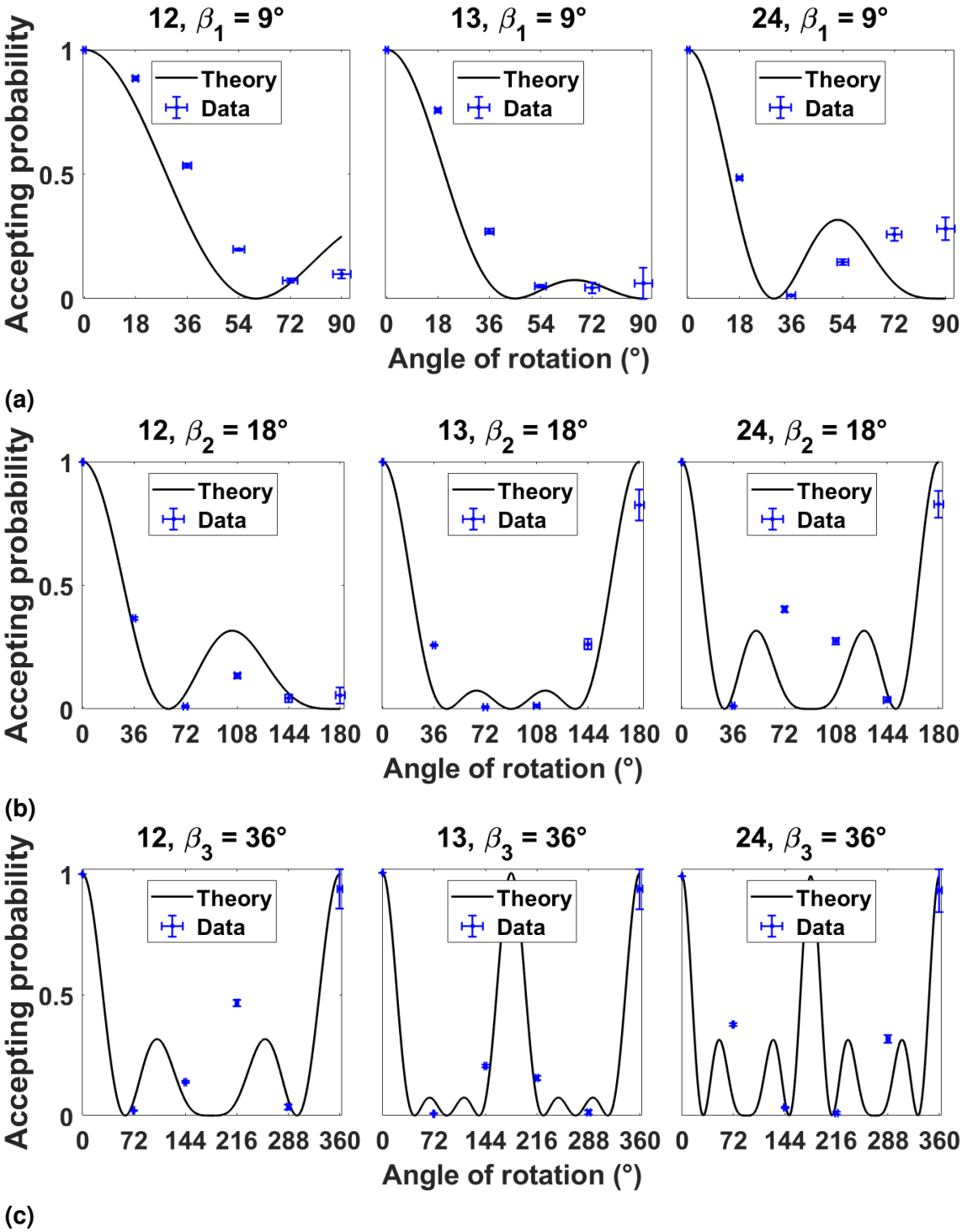

Figure 4.3 Double-qubit measurements for superposed petal modes ($\ell_1 = \pm 1,\ \ell_2 = \pm 2$), ($\ell_1 = \pm 1,\ \ell_2 = \pm 3$), and ($\ell_1 = \pm 2,\ \ell_2 = \pm 4$) with the Dove prism at **(a)** $\beta_1 = 9° \pm 0.5°$,**(b)** $\beta_2 = 18° \pm 0.5°$,and **(c)** $\beta_3 = 36° \pm 0.5°$.

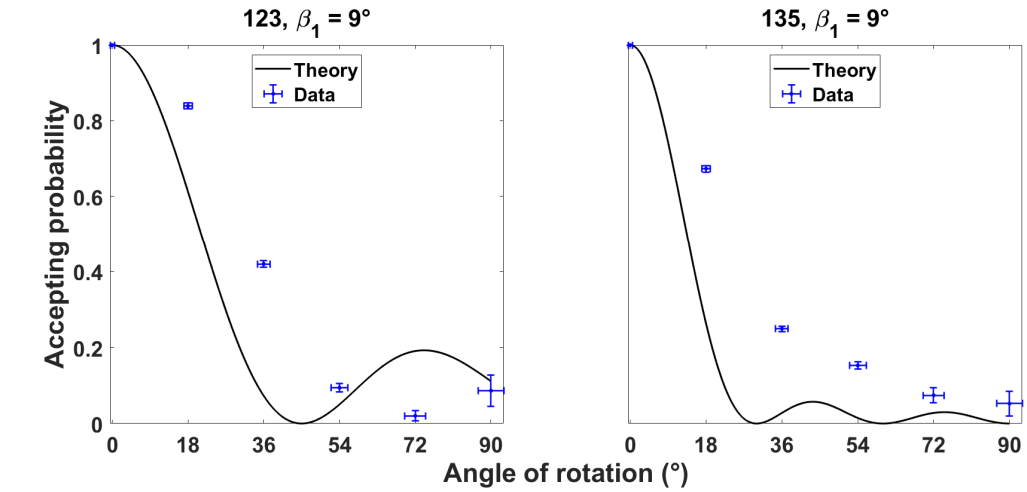

(a)

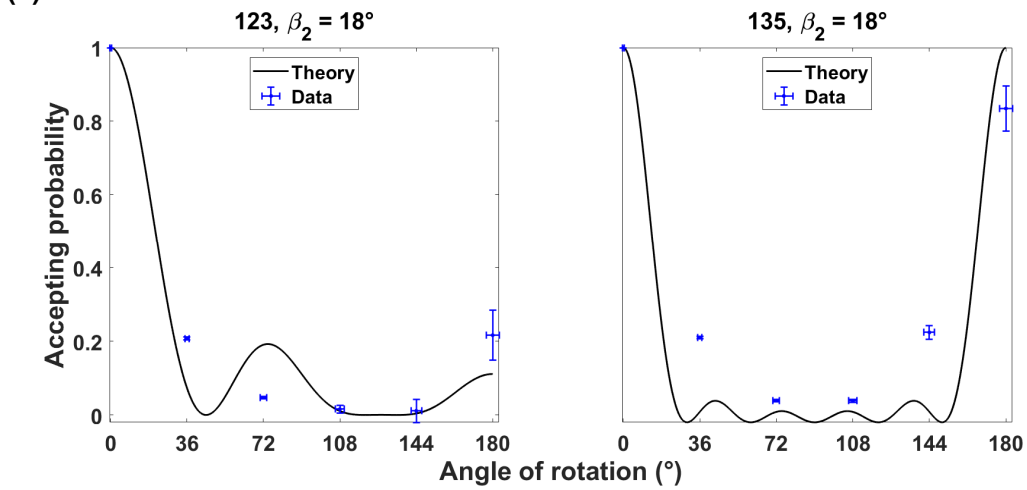

(b)

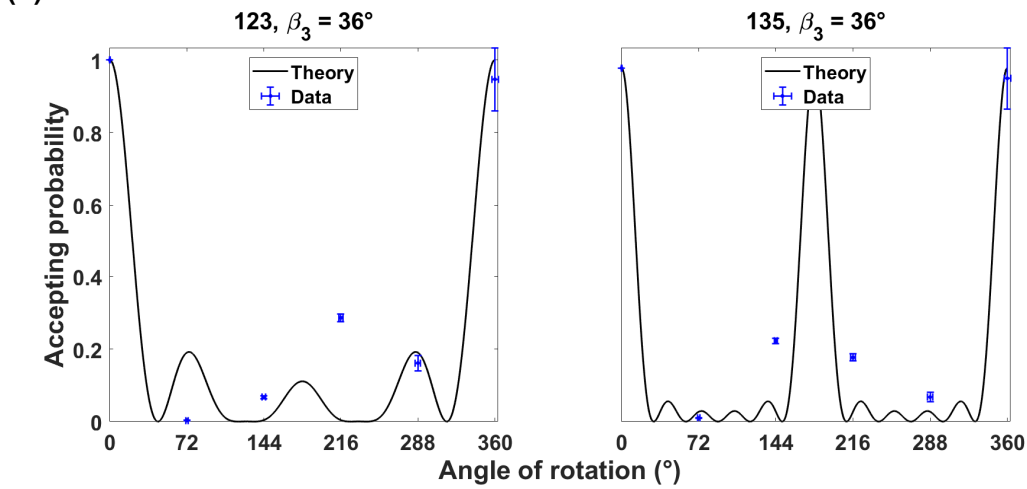

(c)

Figure 4.4 Triple-qubit measurements for superposed petal modes ($\ell_1 = \pm 1,\ \ell_2 = \pm 2,\ \ell_3 = \pm 3$) and ($\ell_1 = \pm 1,\ \ell_2 = \pm 3,\ \ell_3 = \pm 5$) with the Dove prism at **(a)** $\beta_1 = 9° \pm 0.5°$,**(b)** $\beta_2 = 18° \pm 0.5°$,and **(c)** $\beta_3 = 36° \pm 0.5°$.

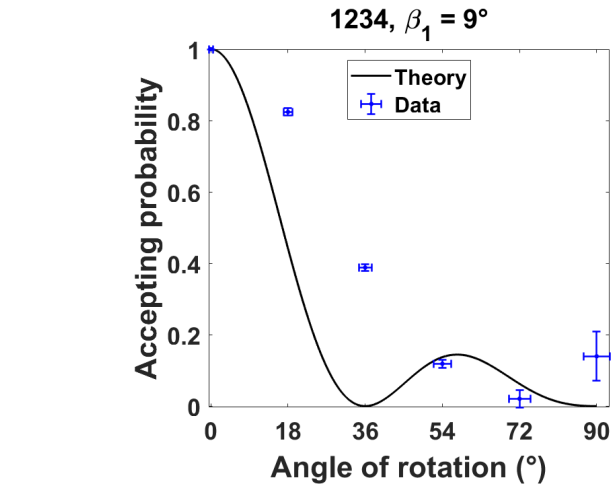

(a)

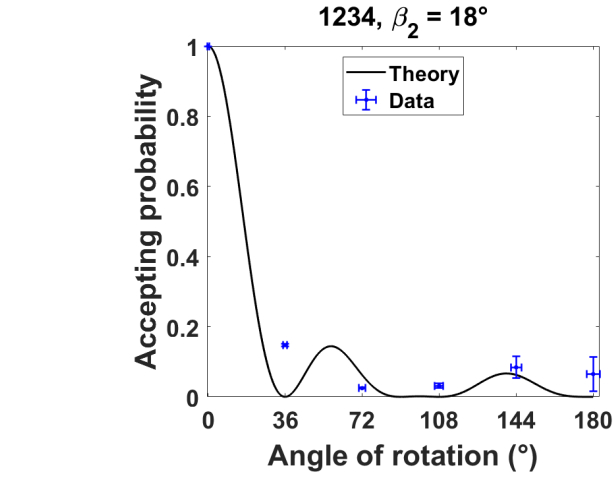

(b)

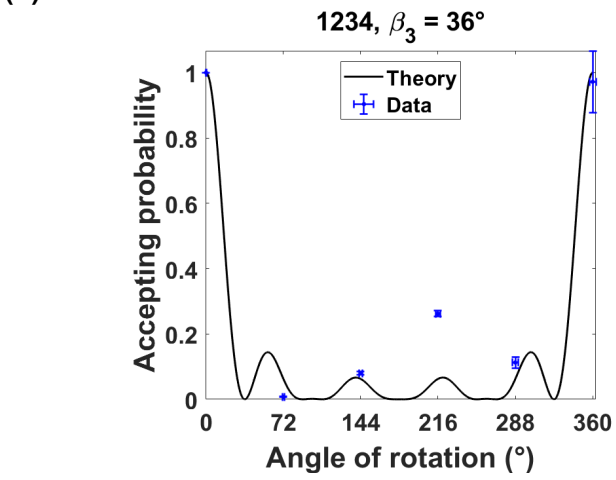

(c)

Figure 4.5 Four-qubit measurements for superposed petal mode ($\ell_1 = \pm 1$, $\ell_2 = \pm 2$, $\ell_3 = \pm 3$, $\ell_4 = \pm 4$) with the Dove prism at **(a)** $\beta_1 = 9° \pm 0.5°$, **(b)** $\beta_2 = 18° \pm 0.5°$, and **(c)** $\beta_3 = 36° \pm 0.5°$.

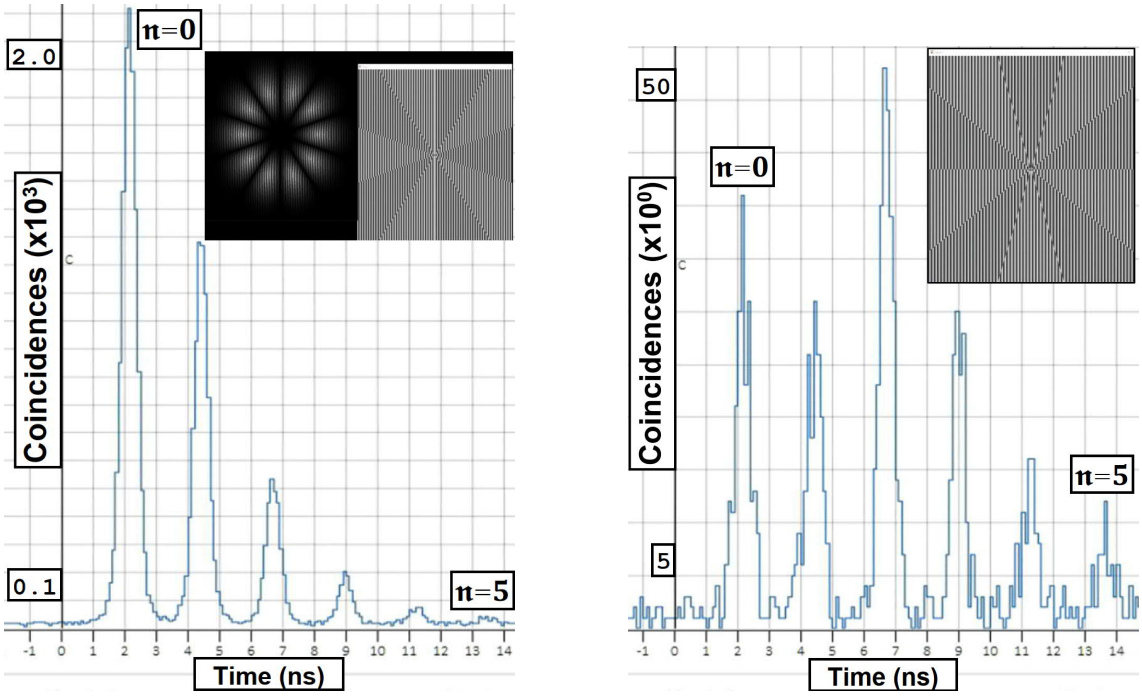

Figure 4.6 Coincidence histograms for single-qubit mode $\ell = \pm 5$ with the Dove prism at $\beta_2 = 18°$. Because the structure rotates by $36°$ per loop, it has rotational symmetry for all $\mathfrak{n}$. **(a)** A phase-flattening measurement shows a near-Gaussian structure similar to that of Figure 4.1. The generated mode is shown in the left half of the SLM screen overlay, and the measurement mask is shown in the right half. **(b)** Measuring for the mode orthogonal to $\ell = \pm 5$, phase-shifted by $180°$, would ideally produce zero counts for all loops or a histogram similar to the Gaussian. Instead, the counts decrease by different fractions for each loop, revealing that loops $\mathfrak{n} \geq 1$ are noisier than loop $\mathfrak{n} = 0$. Note that these screenshots were each taken after about 95% of a 120 s data run, and thus are not representative of final counts.

0 to ensure it was level with the horizontal and plumb with the vertical. It was then repositioned by spinning its rotational mount by hand to visual alignment with β_j on the mount's angular scale. With a more sophisticated method of making the prism level and plumb and/or aligned to β_j, such as laser measurement or a mechanical mount, the angular precision could be improved.

As shown in Figure 4.6, the alignment of successive loops can be examined by comparing the coincidence counts for a petal mode whose lobes align with $2\beta_j$ with the coincidence counts of its orthogonal mode. For $\ell = \pm 5$ with the Dove prism at an angle of $\beta_2 = 18° \pm 0.5°$, the minimum counts do not decrease at the same rate as the maximum counts.

As shown in Figure 4.7, this observation affects the (reciprocal) extinction ratios, E, and visibilities, V, of each loop, which depend on the maximum and minimum counts

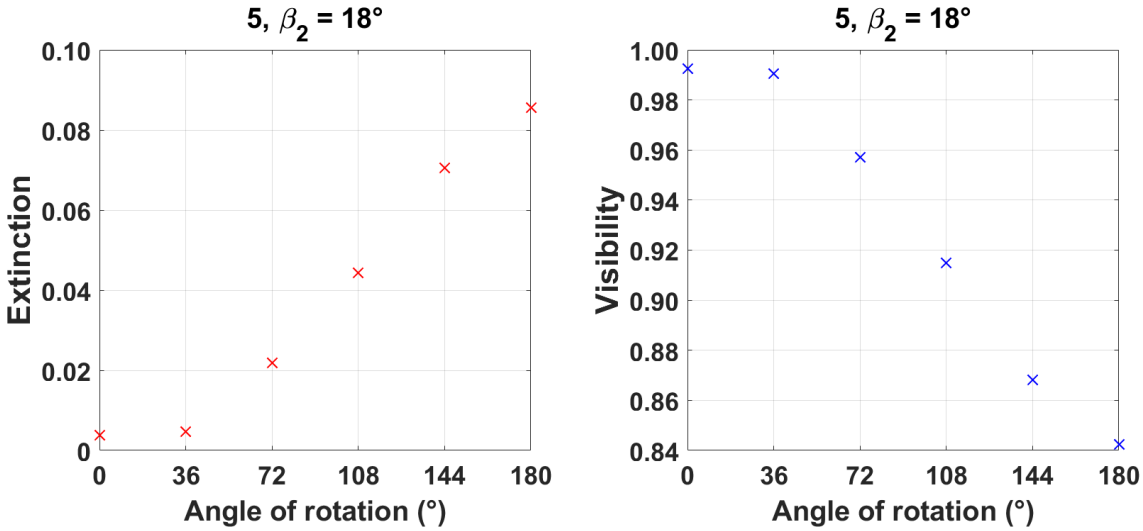

Figure 4.7 Extinction and visibility for $\ell = \pm 5,\ \beta_2 = 18° \pm 0.5°$. **(a)** The reciprocal of the extinction ratio is ideally close to zero, while here it increases by nearly an order of magnitude from the $\mathfrak{n} = 0$ loop to the $\mathfrak{n} = 5$ loop. **(b)** The visibility is ideally near 1, while here it decreases from ~0.99 to ~0.84 over 5 loops.

and accidentals. These quantities are calculated:

$$E_{\mathfrak{n}} = \frac{C_{\mathfrak{n}_{min}}}{C_{\mathfrak{n}_{max}}};\ \ V_{\mathfrak{n}} = \frac{C_{\mathfrak{n}_{max}} - C_{\mathfrak{n}_{min}}}{C_{\mathfrak{n}_{max}} + C_{\mathfrak{n}_{min}}}, \tag{4.9}$$

with $C_{\mathfrak{n}}$ defined in Equation (4.1).

Altogether, this indicates that photons from each loop were hitting the measurement mask at slightly different positions (the center of the beam should align with the center of the holographic pattern), with slightly different **k**-vectors, and/or that the prism angle was not precise enough, causing inaccuracies in the rotation angles. This also explains part of the reason for the decay in the accepting probability of the $\ell = \pm 5,\ \beta_2 = 18° \pm 0.5°$ mode of Figure 4.2b, where each loop has a nominal accepting probability of 1.

Presumably, other qubit states show similar variation, though high-dimensional superposition states have several orthogonal substates which must be measured and accounted for. Such measurements were not done for this thesis, but are possible in further experiments.

The results of Figures 4.3b (except for the mode with $\ell_1 = \pm 1,\ \ell_2 = \pm 2$) and 4.3c show that, while the experiment was unable to investigate the prime number promise problem with $\mathfrak{p} = 11$ using a 4-qubit system with an 8-dimensional state space, a 2-qubit system with a 4-dimensional state space was able to examine the prime number promise problem with $\mathfrak{p} = 5$, demonstrating that it is feasible to achieve low decision errors with state spaces smaller than those required classically.

The next chapter will summarize this thesis and discuss how future investigations can expand on the use of structured photons for multi-qubit QFAs.

5 CONCLUSION

This chapter will summarize the idea, background, and implementation of this thesis, then provide an outlook for future prospects building on this foundation.

5.1 Summary

The motivation for this work was to determine whether heralded single photons could be used as a multi-qubit QFA to conduct prime number searches on the length of an input string more efficiently in terms of state space than a classical FA, which requires a number of states equal to the prime number of interest, $\mathfrak{p}$. Because of the superposition principle, a multi-qubit system can perform similar calculations with exponential state efficiency decided by $\mathcal{O}(\log \mathfrak{p})$.

In three experiments with different parameters, single- and multi-qubit QFAs were constructed using heralded single photons by encoding them with transverse structures described by the high-dimensional state space of LG modes, derived from the solutions of the PWE (Equation (2.11)) in cylindrical coordinates. Using a Dove prism, three different unitary operators were applied to rotate a heralded photon's structure, each representing the act of reading a character from an input string. A beamsplitter loop was used to probabilistically separate strings of different lengths into different time bins, using the heralding photon as a reference to generate coincidence histograms that could be gauged according to a baseline histogram of the Gaussian state, enabling the calculation of accepting probabilities for input strings of different lengths. The maximum loop number (input string length) that could be measured experimentally was 5, so the prime number $\mathfrak{p} = 5$ was analyzed.

In the first experiment, a rotation of $18°$ was applied to the photon in each loop; in the second, the rotation angle was $36°$; and in the third, it was $72°$. The final angles after $\mathfrak{n} = 5$ loops were then $90°$, $180°$, and $360°$, respectively. It was observed that each rotational operator produced different results for structures with different rotational symmetries. Several of these multi-qubit states produced convincing results for the principle of using complex-structured photons as multi-qubit QFAs to pursue the prime number promise problem. It was observed that only the 2-qubit (4 basis state) structures with $180°$ and $360°$ symmetry demonstrated exponential state efficiency compared to a classical FA requiring $\mathfrak{p} = 5$ states for the same problem, but more efficient systems will in principle enable the search to continue for $\mathfrak{p} = 7$, $\mathfrak{p} = 11$, etc.

5.2 Outlook

With the principle of multi-qubit QFAs demonstrated using structured photons, how can future experiments expand on these results and apply them in novel ways?

One modification that could readily be made is the use of a different (not $50{:}50$) beamsplitter. As mentioned in Chapter 3, the equation governing the probability for a photon to leave a beamsplitter loop after $\mathfrak{n} \geq 1$ loops is, for a general $R{:}T$ beamsplitter, $P_{\mathfrak{n}}^{B} = t^2(r^{\mathfrak{n}-1})$. The efficiency of different beamsplitters for different loop numbers can therefore readily be analyzed. For example, a $70{:}30$ beamsplitter has a higher calculated efficiency than a $50{:}50$ beamsplitter for loop numbers $5 \leq \mathfrak{n} \leq 7$, and an $80{:}20$ beamsplitter has the highest calculated efficiency for loop numbers $8 \leq \mathfrak{n} \leq 12$. For $\mathfrak{n} \geq 13$, a $90{:}10$ beamsplitter is most efficient.

The efficiency of the Type II SPDC source is also a factor. The Experimental Quantum Optics group has seen efficiencies (coincidences to singles ratios) near 48% using similar setups, but the source was rebuilt for this thesis and saw an efficiency of 13%. A 3- or 4-fold increase in efficiency would presumably allow the resolution of higher loop numbers, bringing the possibility of investigating larger prime numbers into reach.

Having conducted a fascinating investigation into the field of quantum computing using photons with complex structures as multi-qubit quantum finite automata, it will be exciting to continue to attend to further developments in this and related fields as we learn about the physics of our universe.

REFERENCES

[1] L. Allen, M. W. Beijersbergen, R. J. C. Spreeuw, and J. P. Woerdman. Orbital angular momentum of light and the transformation of Laguerre-Gaussian laser modes. *Phys. Rev. A* **45**.8185 (1992). DOI: 10.1103/PhysRevA.45.8185.

[2] A. Amainis and R. Freivalds. 1-Way Quantum Finite Automata: Strengths, Weaknesses and Generalizations. *FOCS* (1998), 332–341. DOI: 10.5555/795664.796424.

[3] D. L. Andrews and M. Babiker. *The Angular Momentum of Light*. New York: Cambridge University Press, 2013. ISBN: 978-1-107-00634-8. DOI: 10.1201/9781482285840.

[4] R. Bach. *Jonathan Livingston Seagull*. USA: Macmillan, 1970. ISBN: 978-0684846842.

[5] E. Bolduc, N. Bent, E. Santamato, and R. W. Boyd. Exact solution to simultaneous intensity and phase encryption with a single phase-only hologram. *Optics Letters* **38**.18 (2013), 3546–3549. DOI: 10.1364/OL.38.003546.

[6] D. C. Burnham and D. L. Weinberg. Observation of Simultaneity in Parametric Production of Optical Photon Pairs. *Phys. Rev. Lett.* **25**.84 (1970). DOI: 10.1103/PhysRevLett.25.84.

[7] P. A. M. Dirac. *The Principles of Quantum Mechanics*. International series of monographs on physics. Oxford: Clarendon Press, 1981. ISBN: 978-0-198-52011-5.

[8] A. Einstein (translated by I. Born). *The Born-Einstein letters*. New York: Walker and Co., 1971. ISBN: 978-0-8027-0326-2.

[9] M. Erhard, R. Fickler, and M. K. *et al.* Twisted photons: new quantum perspectives in high dimensions. *Light Sci Appl* **7**.17146 (2018). DOI: 10.1038/lsa.2017.146.

[10] R. Ficker. *Quantum Entanglement of Complex Structures of Photons*. PhD thesis. University of Vienna, 2015. ISBN: 978-3-319-22230-1. DOI: 10.1007/978-3-319-22231-8.

[11] N. Gonzalez, G. Molina-Terriza, and J. P. Torres. How a Dove prism transforms the orbital angular momentum of a light beam. *Optics Express* **14**.20 (2006). DOI: 10.1364/OE.14.009093.

[12] C. K. Hong and L. Mandel. Experimental realization of a localized one-photon state. *Phys. Rev. Lett.* 56 (1 1986), 58–60. DOI: 10.1103/PhysRevLett.56.58.

[13] A. Kondacs and J. Watrous. On the Power of Quantum Finite State Automata. *Proceedings of the 38th IEEE Conference on Foundations of Computer Science* (1997), 66–75. DOI: 10.1109/SFCS.1997.646084.

[14] N. K. Langford. *Encoding, manipulating and measuring quantum information in optics*. PhD thesis. University of Queensland, 2007.

[15] M. V. Lawson. *Finite Automata*. New York: Chapman and Hall/CRC, 2004. ISBN: 978-1-58488-255-8. DOI: 10.1201/9781482285840.

[16] M. J. Padgett and J. P. Lesso. Dove prisms and polarized light. *Journal of Modern Optics* **46**.2 (1999), 175–179. DOI: 10.1080/09500349908231263.

[17] M. E. Peskin. *An Introduction to Quantum Field Theory*. New York: Avalon Publishing, 1995. ISBN: 978-0201503975.

[18] M. O. Rabin. Probabilistic Automata. *Information and Control* **6**.3 (1963), 230–245. DOI: 10.1016/S0019-9958(63)90290-0.

[19] M. O. Rabin and D. Scott. Finite Automata and Their Decision Problems. *IBM Journal of Research and Development* **3**.2 (1959), 114–125. DOI: 10.1147/rd.32.0114.

[20] A. E. Siegman. *Lasers*. University Science Books, 1986. ISBN: 978-0-9357-0211-8.

[21] M. Sipser. *Introduction to the Theory of Computation, 3rd edition*. United States of America: Cengage Learning, 2013. ISBN: 978-1133187790.

[22] J. Watrous. Encyclopedia of Complexity and System Science. Also available at arXiv:0804.3401. Springer, 2009. Chap. Quantum computational complexity. ISBN: 978-0-387-75888-6.

[23] H. Weyl (translated by H. P. Robertson). *The Theory of Groups and Quantum Mechanics*. New York: Dover, 1950. ISBN: 978-0-486-60269-1.

[24] Z. Zhang, Z. You, and D. Chu. Fundamentals of phase-only liquid cystal on silicon (LCOS) devices. *Light Sci Appl* **3**.e213 (2014). DOI: 10.1038/lsa.2014.94.